Supporting Information

Intramolecular Charge Transfer Assisted Multi-Resonance Thermally Activated Delayed Fluorescence Emitters for High-Performance Solution-Processed Narrowband OLEDs

Zhi Yang,[a] Shengyu Li,[a] Lei Hua,[b] Shian Ying,[a] Yuchao Liu*,[a] Zhongjie Ren*,[c] Shouke Yan*[a] [c]

[a] *Z. Yang, S. Li, Dr. S. Ying, Dr. Y. Liu, Prof. S. Yan*
Department Key Laboratory of Rubber-Plastics, Ministry of Education/Shandong Provincial Key Laboratory of Rubber-Plastics, School of Polymer Science and Engineering, Qingdao University of Science & Technology, Qingdao 266042, P. R. China.
E-mail: liuyc@qust.edu.cn skyan@qust.edu.cn

[b] *Dr. L. Hua*
School of Materials Science & Engineering, Changzhou University, Changzhou 213164, P. R. China.

[c] *Prof. Z. Ren*
State Key Laboratory of Chemical Resource Engineering, College of Materials Science and Engineering, Beijing University of Chemical Technology, Beijing 100029, P. R. China.
E-mail: renzj@buct.edu.cn

Contents

S1. Materials and experimental procedures

All the reagents were purchased from *J&K Scientific*, *Energy Chemical*, *Sigma-Aldrich* and used without further purification, unless otherwise noted. The solvents were purchased from *Sinopharm Chemical Reagent Co., Ltd.*, and anhydrous toluene was gained through sodium reflux. The NMR spectra were performed using a Bruker AVAN CE NEO 400 spectrometer (400MHz). ^{1}H NMR and ^{13}C NMR spectra were obtained with chloroform-*d* was adopted as slovent and TMS as internal standard, respectively. Electron spray mass spectra data (ESI-MS) were collected on Xevo G2 Qtof. Cyclic voltammetry (CV) was performed in nitrogen-bubbled acetonitrile solvent using CHI voltammetric analyser at room temperature. Tetrabutylammonium hexafluorophosphate ($TBAPF_6$ 0.1 M) was adopted as the electrolyte, and a glassy carbon working electrode, a platinum wire auxiliary electrode, and an $Ag/AgNO_3$ pseudo-reference electrode were used in the conventional three-electrode system. Cyclic voltammograms were performed from 0 V to 1.5 V at scan rate of 100 mV s^{-1}, and ferrocene power as internal standard was added into system[1,2]. Then the HOMO energy levels could be calculated according to the internal reference ferroceneredox couple in acetonitrile by using the following formulas:[3]

$$E_{HOMO} = -\left(E_{(onset,ox\ vs\ Fc^{+}/Fc)} + 4.8\right)$$

The LUMO energy levels could be calculated by the HOMO values and the energy gap (E_gs) obtained from the onset of the absorption spectra of the emitters.

Differential scanning calorimetry (DSC) was performed on a TA Q2000 differential scanning calorimeter at a heating rate of 10 °C min^{-1} from 30 to 300 °C and a cooling rate of 10 °C min^{-1} from 300 to 30 °C under nitrogen atmosphere. The glass transition temperature (T_g) and the melting temperature (T_m) were determined from the second heating scan. Thermogravimetric analysis (TGA) was performed with a METTLER TOLEDO TGA/DSC 1/1100SF instrument. The thermal stability of the samples was obtained by measuring their 5% weight loss while heating at a rate of 10 °C min^{-1} from 25 to 800 °C under a nitrogen atmosphere.

UV/Vis absorption spectra were recorded on a Hitachi U-2910 spectrophotometer. PL spectra, including fluorescence at 77 K, and phorescence at 77 K, were recorded on a Hitachi F-7000 fluorescence spectrophotometer, and the energy gap (ΔE_{ST}) between lowest singlet (S_1) and triplet excited states (T_1) were determined from the difference values of the onset positions of fluorescencent and phorescencent spectra. To gain the

proportion of delayed fluorescence (DF), the steady-state PL spectra in vacuum and in air, were performed using FS-5 spectrometer from Edinburgh Instruments Limited with Xe lamp source. The photoluminance quantum yields of the blended films were measured on FLS-980 with an integrating sphere (φ = 150 mm) under nitrogen gas. The transient-state PL spectra in vacuum and in air, including prompt fluorescence (PF) and DF spectra, and the temperature dependence of transient PL decay curves were determined using nanosecond gated luminescence and lifetime measurements with a high-energy pulsed Nd:YAG laser emitting at 320 nm.

S2. Computational Methods

All the density functional theory (DFT) calculations were carried out using Gaussian 16 package. The ground-state geometry was fully optimized using DFT with PBE1PBE hybrid functional at the basis set level of 6-311G**. The excited-state properties were obtained by time-dependent density functional theory (TD-DFT) at the basis set level of PBE1PBE/6-311G**. In addition, the overlaps between the hole and electron density distributions in the S_1 and T_1 states were extracted by the Multiwfn code and visualized using VMD[4, 5].

The reorganization energy is gained by the geometrical deformation in the Franck-Condon vertical absorption transition and radiative process, and the value can be estimated using the four-point approach. Based on the data obtained from Gaussian16 package, the frequency analysis of reorganization energies and Huang–Rhys factors combined with Gaussian 16 FCHT output data processing[6].

The molecular dynamics (MD) simulation was performed by GROMACS software package (version 2023.2) using general Amber force field (GAFF) and restrained electrostatic potential (RESP) atomic charge. Firstly, molecules were randomly placed into a cubic simulation box. Then, the box was annealed from 0 K to 500 K and reduced to 298 K within 900 ps and then the system was pre-equilibrated for 1300 ps with periodic boundary conditions using NPT ensemble at 298 K. Finally, the system was equilibrated for 2 ns using NPT ensemble at 298 K[7].

S3. Device Fabrication and Measurement

Glass substrates pre-coated with a 100-nm-thin layer of indium tin oxide (ITO) with a sheet resistance of 20 Ω per square were thoroughly cleaned in ultrasonic bath of washing liquor, deionized water and isopropyl alcohol. Then, the substrates were totally dried in a 120 °C oven. Then the ITO substrates were treated by air plasma for 8 minutes. The hole transportation layer was firstly performed by spin coating PSS: PEDOT 4083 on ITO substrates with 40 nm thickness. After that, the ITO substrates were transferred into glovebox. After heat treated for another 30 min at 120 °C, the emissive layer was spin-coated on hole transportation layer with 40 nm thickness. The precursor solution of emissive layer consists of 10 mg/mL emitter and host materials dissolved in anhydrous chlorobenzene. After heat treated for another 30 min at 60 °C, the ITO substrates were moved to vacuum evaporation chamber, and the residual functional layers were deposited sequentially by high-vacuum (<1.0 × 10^{-5} Pa) thermal evaporation onto a glass substrate pre-coated with hole transportation and emissive layers. The thermal deposition rates for the electron transportation, LiF and Al layers were 2.0-2.5, 0.15 and 1~5 Å s^{-1}, respectively. The active area of each device was 0.0625 cm^2, and each device has four pixels. The electroluminescence spectra, the current density-voltage characteristics and the current density-voltage-luminance curves characterizations of the OLEDs were carried out with a Photo Research Spectra Scan PR-670 Spectroradiometer and a Keithley 2400 Source Meter and they are recorded simultaneously. All measurements were done at room temperature under ambient conditions.

S4. Analysis of rate constants

Time-resolved transient photoluminescence decay measurements were utilized to study the delayed fluorescence phenomenon of the molecule in doped films (2 wt% in PhCzBCz), Rate constants of different kinetic processes were calculated following the equations (S1)-(S3) below:

Where k_r^S, k_{nr}^S, k_{RISC} represent the rate constant of singlet radiative decay, non-

radiative decay of singlet radiative decay, and reverse intersystem crossing, respectively; $\emptyset_{PL}$, φ_{DF}, τ_p and τ_d represent total PLQY, quantum yield of the delayed component, lifetimes of the prompt and delayed components, respectively.

In this study, φ_{DF} and the quantum yield of the delayed component (φ_{PF}) were determined by using the total PLQY and the integrated intensity ratio between prompt and delayed components which was calculated from transient photoluminescence measurements as equations (S4)-(S6) below:

$$k_{RISC} = \emptyset_{PL}/[\tau_d(1-\varphi_{DF})] \quad \text{S1}$$

$$k_r^S = (1-\varphi_{DF})/\tau_p \quad \text{S2}$$

$$k_{nr}^S = k_r^S \times (1-\emptyset_{PL})/\emptyset_{PL} \quad \text{S3}$$

$$I(t) = A_p e^{-\frac{t}{\tau_p}} + A_d e^{-\frac{t}{\tau_d}} \quad \text{S4}$$

$$\varphi_{PF} = \frac{A_p\tau_p}{A_p\tau_p + A_d\tau_d} \quad \text{S5}$$

$$\varphi_{DF} = \frac{A_d\tau_d}{A_p\tau_p + A_d\tau_d} \quad \text{S6}$$

S5. Synthesis and Characteristics

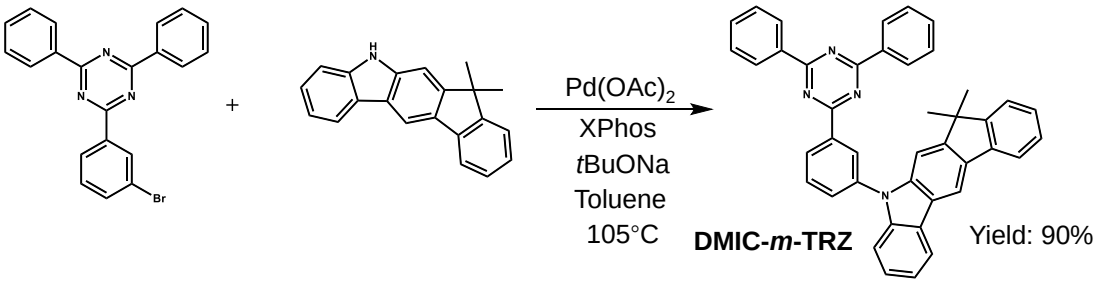

Scheme S1. Synthesis route of DMIC-*m*-TRZ.

2-(3-Bromophenyl)-4,6-diphenyl-1,3,5-triazine (1.55 g, 4 mmol), 5,7-dihydro-7,7-dimethylindeno[2,1-b]carbazole (1.25 g, 4.4 mmol), $Pd(OAc)_2$ (0.045 g, 0.2 mmol), XPhos (0.19 g, 0.4 mmol), *t*BuONa (0.58 g, 6 mmol), were dissolved in anhydrous toluene (30 mL) under a nitrogen atmosphere. After stirring at 105 °C for 12 h, the reaction was cooled down to room temperature. Then the mixture was extracted with

dichloromethane/water for three times, and then organic layer was dehydrated with anhydrous magnesium sulfate. After filtering and drying, crude product could be obtained. The crude product was purified by column chromatography (the eluent was dichloromethane: petroleum ether = 1:5), and the pale yellow powder (2.13 g) was obtained with a yield of 90%.

^{1}H NMR (400 MHz, Chloroform-*d*) δ 9.04 (dt, *J* = 1.8, 1.1 Hz, 1H), 8.92–8.86 (m, 1H), 8.79–8.72 (m, 4H), 8.49 (d, *J* = 0.7 Hz, 1H), 8.24 (dt, *J* = 7.7, 1.0 Hz, 1H), 7.91 – 7.82 (m, 3H), 7.61–7.48 (m, 8H), 7.45–7.26 (m, 5H), 1.53 (s, 6H).

^{13}C NMR (101 MHz, Chloroform-*d*) δ 171.88, 171.02, 153.39, 153.34, 141.30, 141.20, 139.71, 138.55, 138.41, 135.97, 132.72, 132.60, 130.96, 130.34, 129.02, 128.69, 127.87, 127.59, 127.10, 126.37, 125.83, 123.78, 123.13, 122.59, 120.25, 120.21, 119.42, 111.43, 109.81, 104.02, 46.85, 27.99.

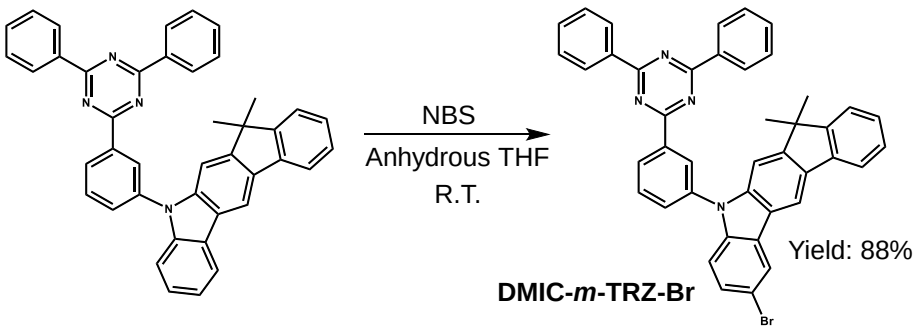

Scheme S2. Synthesis route of DMIC-*m*-TRZ-Br.

DMIC-*m*-TRZ (1.18 g, 2 mmol) was dissolved in anhydrous THF (20 mL), and then NBS (0.37 g, 2.1 mmol) dissolved in in anhydrous THF (20 mL) was added into reaction system. After the mixture was stirring at room temperature for 12 h. Then the mixture was extracted with dichloromethane/water for three times, and then organic layer was dehydrated with anhydrous magnesium sulfate. After filtering and drying, crude product could be obtained. The crude product was purified by column chromatography (the eluent was dichloromethane: petroleum ether = 1:5), and the pale-yellow powder (1.18 g) was obtained with a yield of 88%.

^{1}H NMR (400 MHz, Chloroform-*d*) δ 8.86 (t, *J* = 1.8 Hz, 1H), 8.75 (dt, *J* = 7.6, 1.6

Hz, 1H), 8.68–8.64 (m, 4H), 8.30–8.25 (m, 2H), 7.80 (d, *J* = 7.5 Hz, 1H), 7.72–7.62 (m, 2H 7.51–7.34 (m, 10H),7.25 (dd, *J* = 7.9, 6.6 Hz, 2H), 1.48 (s, 6H).

^{13}C NMR (101 MHz, Chloroform-*d*) δ 171.80, 170.81, 154.08, 153.33, 141.40, 139.85, 139.43, 138.62, 137.90, 135.92, 133.05, 132.75, 130.60, 130.38, 129.04, 128.69, 128.47, 128.08, 127.27, 127.26, 126.68, 125.58, 123.07, 122.66, 122.10, 119.60, 113.07, 111.64, 111.27, 104.24, 46.93, 28.02.

HRMS (MALDI-TOF): m/z calculated for $C_{42}H_{30}BrN_4$ $[M+H]^+$: 669.1648; Found: 669.1643.

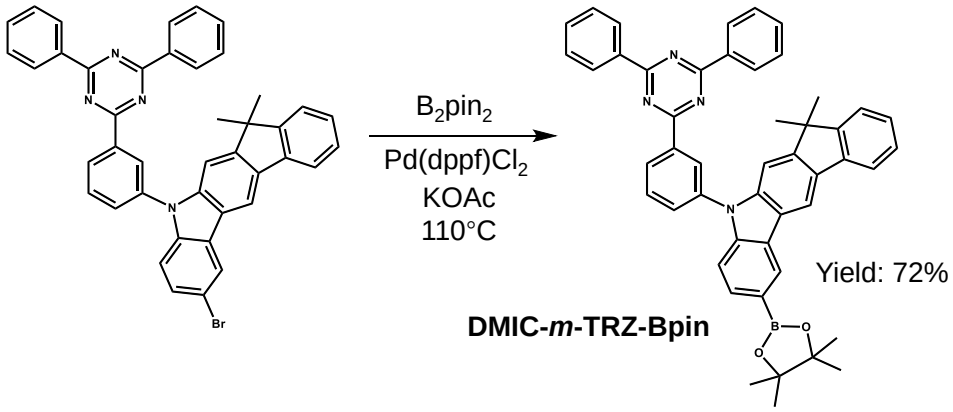

Scheme S3. Synthesis route of DMIC-*m*-TRZ-Bpin.

DMIC-*m*-TRZ-Br (1.00 g, 1.5 mmol), B_2pin_2 (0.76 g, 3 mmol), Pd (dppf)Cl_2 (0.055 g, 0.075 mmol), KOAc (0.44 g, 4.5 mmol), were dissolved in anhydrous 1,4-dioxane (30 mL) under a nitrogen atmosphere. After stirring at 110 °C for 12 h, the reaction was cooled down to room temperature. Then the mixture was extracted with dichloromethane/water for three times, and then organic layer was dehydrated with anhydrous magnesium sulfate. After filtering and drying, crude product could be obtained. The crude product was purified by column chromatography (the eluent was ethyl acetate: petroleum ether = 1:10), and the white powder (0.77 g) was obtained with a yield of 72%.

^{1}H NMR (400 MHz, Chloroform-*d*) δ 8.95 (q, *J* = 1.5 Hz, 1H), 8.82 (pd, *J* = 4.3, 1.6 Hz, 1H), 8.70–8.65 (m, 5H), 8.47 (s, 1H), 7.83–7.75 (m, 4H), 7.53–7.38 (m, 8H), 7.36–7.29 (m, 2H), 7.21 (td, *J* = 7.4, 1.1 Hz, 1H), 1.45 (s, 6H), 1.35 (s, 12H).

^{13}C NMR (101 MHz, Chloroform-*d*) δ 171.89, 171.00, 153.38, 153.29, 143.37, 141.32, 139.66, 138.58, 138.20, 135.96, 132.90, 132.71, 132.28, 130.97, 130.38, 129.02, 128.69, 128.03, 127.67, 127.59, 127.14, 126.40, 123.47, 123.31, 122.56, 119.38, 111.67, 109.18, 104.06, 83.71, 77.34, 46.85, 27.94, 25.00.

HRMS (MALDI-TOF): m/z calculated for $C_{48}H_{42}BN_4O_2$ $[M+H]^+$: 717.3395; Found: 717.3399.

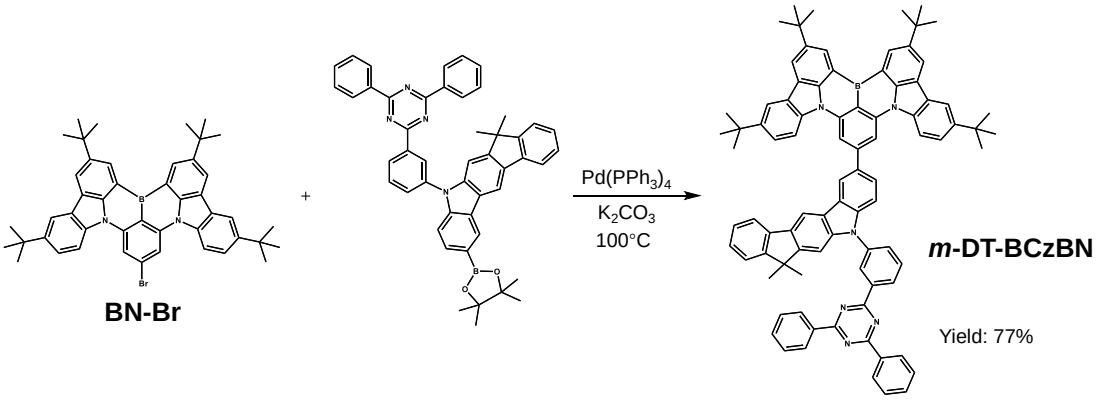

Scheme S4. Synthesis route of *m*-DT-BCzBN.

10-bromo-2,5,15,18-tetrakis(1,1-dimethylethyl)-indolo[3,2,1-de]indolo[3',2',1':8,1][1,4]benzazaborino[2,3,4-kl]phenazaborine (BN-Br) (0.72 g, 1.0 mmol), **DMIC-*m*-TRZ-Bpin** (0.75 g, 1.05 mmol), $Pd(PPh_3)_4$ (0.058 g, 0.05 mmol), K_2CO_3 (0.21g, 1.5 mmol) were dissolved in anhydrous toluene (30 mL) / deionized water (10 mL) under a nitrogen atmosphere. After stirring at 100 °C for 24 h, the reaction was cooled down to room temperature. Then the mixture was extracted with dichloromethane/water for three times, and then organic layer was dehydrated with anhydrous magnesium sulfate. After filtering and drying, crude product could be obtained. The crude product was purified by column chromatography (the eluent was dichloromethane: petroleum ether = 1:5), and the bright yellow powder (0.95 g) was obtained with a yield of 77%.

^{1}H NMR (400 MHz, Chloroform-*d*) δ 9.13 (dd, *J* = 6.8, 1.9 Hz, 3H), 8.92 (dt, *J* = 7.6, 1.5 Hz, 1H), 8.74 (ddd, *J* = 7.2, 3.1, 1.5 Hz, 5H), 8.70–8.64 (m, 3H), 8.54–8.45 (m, 4H), 8.28 (d, *J* = 2.0 Hz, 2H), 8.03 (dd, *J* = 8.5, 1.8 Hz, 1H), 7.98–7.87 (m, 3H), 7.73 (d, *J* = 8.4 Hz, 1H), 7.68–7.48 (m, 9H), 7.47–7.38 (m, 2H), 7.31 (td, *J* = 7.4, 1.1 Hz, 1H), 1.69

(s, 18H), 1.57 (s, 6H), 1.52 (s, 18H).

^{13}C NMR (101 MHz, Chloroform-*d*) δ 171.84, 170.90, 153.79, 153.38, 147.27, 145.25, 144.72, 144.57, 141.82, 141.79, 141.33, 139.55, 138.65, 138.39, 138.24, 135.90, 134.53, 132.96, 132.69, 130.88, 130.43, 129.81, 128.97, 128.64, 128.05, 127.55, 127.16, 126.50, 126.08, 124.56, 124.42, 123.58, 123.21, 122.59, 121.80, 121.77, 121.74, 121.72, 120.54, 119.55, 117.29, 114.23, 111.77, 110.45, 107.64, 104.31, 46.91, 35.19, 34.80, 32.23, 31.83, 27.98.

MS (MALDI-TOF): m/z calculated for $C_{88}H_{77}BN_6$ $[M]^+$: 1228.6303; Found: 1228.3051.

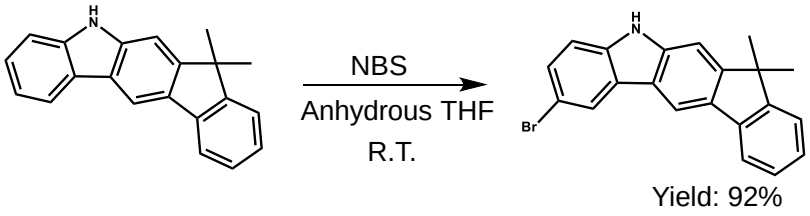

Scheme S5. Synthesis route of DMIC-Br.

5,7-Dihydro-7,7-dimethylindeno[2,1-b]carbazole (1.42 g, 5.0 mmol) was dissolved in anhydrous THF (30 mL), and then NBS (0.91 g, 5.1 mmol) dissolved in in anhydrous THF (20 mL) was added into reaction system. After the mixture was stirring at room temperature for 12 h, the mixture was extracted with dichloromethane/water for three times, and then organic layer was dehydrated with anhydrous magnesium sulfate. After filtering and drying, crude product could be obtained. The crude product named **DMIC-Br** was purified by column chromatography (the eluent was dichloromethane: petroleum ether = 1:10), and the white powder (1.67 g) was obtained with a yield of 92%.

^{1}H NMR (400 MHz, DMSO-d_6) δ 11.46 (s, 1H), 8.60 (s, 1H), 8.38 (d, J = 1.6 Hz, 1H), 7.84 (dt, J = 7.5, 0.9 Hz, 1H), 7.60 (d, J = 0.8 Hz, 1H), 7.55–7.52 (m, 1H), 7.48 (dd, J = 2.9, 1.3 Hz, 2H), 7.36 (td, J = 7.4, 1.2 Hz, 1H), 7.26 (td, J = 7.4, 1.1 Hz, 1H), 1.51 (s, 6H).

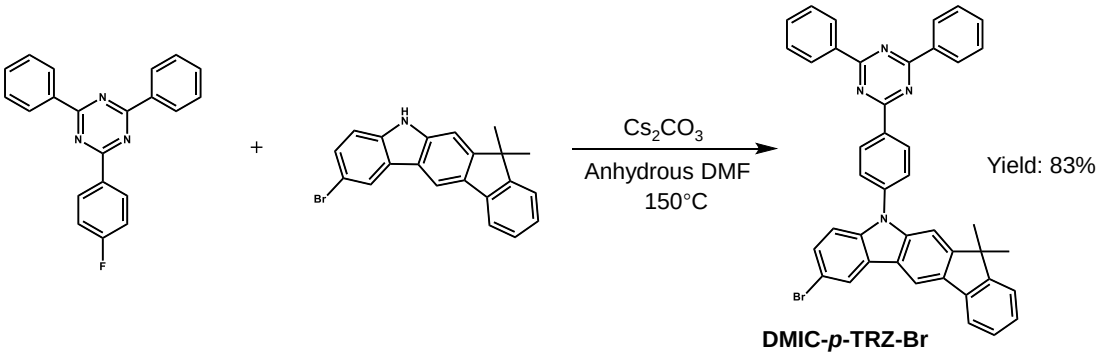

Scheme S6. Synthesis route of DMIC-*p*-TRZ-Br.

2-Bromo-5,7-dihydro-7,7-dimethylindeno[2,1-b]carbazole (1.09 g, 3 mmol), 2-(4-fluorophenyl)-4,6-diphenyl-1,3,5-triazine (1.08 g, 3.3 mmol), and Cs_2CO_3 (1.47 g, 4.5 mmol) were dissolved in anhydrous DMF (40 mL) under a nitrogen atmosphere. After stirring at 150 °C for 12 h, the reaction was cooled down to room temperature. Then the mixture was extracted with dichloromethane/water for three times, and then organic layer was dehydrated with anhydrous magnesium sulfate. After filtering and drying, crude product could be obtained. The crude product was purified by column chromatography (the eluent was dichloromethane: petroleum ether = 1:5), and the pale-yellow powder (1.67 g) was obtained with a yield of 83%.

^{1}H NMR (400 MHz, Chloroform-*d*) δ 8.94 (d, *J* = 8.1 Hz, 2H), 8.77 (d, *J* = 7.3 Hz, 4H), 8.32–8.22 (m, 2H), 7.78 (d, *J* = 7.5 Hz, 1H), 7.70 (d, *J* = 8.1 Hz, 2H), 7.58 (dq, *J* = 14.4, 7.0 Hz, 6H), 7.49–7.42 (m, 2H), 7.33 (tt, *J* = 24.4, 7.4 Hz, 4H), 1.50 (s, 6H).

^{13}C NMR (101 MHz, Chloroform-*d*) δ 171.86, 170.84, 154.11, 153.31, 141.21, 141.09, 139.55, 139.25, 136.07, 135.34, 133.25, 132.75, 130.82, 129.04, 128.75, 128.47, 127.19, 126.80, 126.69, 125.76, 123.03, 122.62, 122.23, 119.52, 113.23, 111.55, 111.40, 104.31, 46.90, 29.73.

HRMS (MALDI-TOF): m/z calculated for $C_{42}H_{30}BrN_4$ $[M+H]^+$: 669.1648; Found: 669.1651.

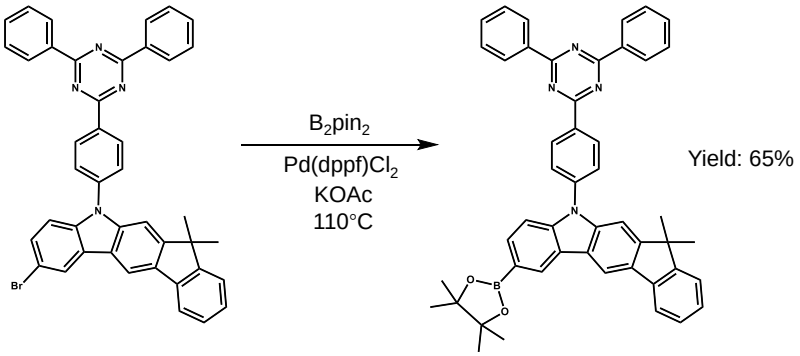

Scheme S7. Synthesis route of DMIC-*p*-TRZ-Bpin.

DMIC-*p*-TRZ-Br (1.00 g, 1.5 mmol), B_2pin_2 (0.76 g, 3 mmol), $Pd(dppf)Cl_2$ (0.055 g, 0.075 mmol), KOAc (0.44 g, 4.5 mmol), were dissolved in anhydrous 1,4-dioxane (30 mL) under a nitrogen atmosphere. After stirring at 110 °C for 12 h, the reaction was cooled down to room temperature. Then the mixture was extracted with dichloromethane/water for three times, and then organic layer was dehydrated with anhydrous magnesium sulfate. After filtering and drying, crude product could be obtained. The crude product was purified by column chromatography (the eluent was ethyl acetate: petroleum ether = 1:10), and the white powder (0.70 g) was obtained with a yield of 65%.

^{1}H NMR (400 MHz, Chloroform-*d*) δ 9.07 (d, *J* = 7.8 Hz, 2H), 8.84 (d, *J* = 7.0 Hz, 4H), 8.73 (s, 1H), 8.52 (s, 1H), 7.87 (dt, *J* = 16.3, 8.2 Hz, 4H), 7.63 (t, *J* = 8.0 Hz, 6H), 7.53 (d, *J* = 8.5 Hz, 2H), 7.47–7.36 (m, 2H), 7.30 (t, *J* = 7.4 Hz, 1H), 1.54 (s, 6H), 1.43 (s, 12H).

^{13}C NMR (101 MHz, Chloroform-*d*) δ 171.82, 170.93, 153.42, 153.32, 142.99, 141.59, 140.91, 139.56, 136.09, 135.14, 133.13, 132.77, 132.33, 130.91, 129.24, 128.82, 127.68, 127.15, 127.01, 126.48, 123.71, 123.53, 122.57, 119.41, 111.69, 109.39, 104.27, 83.75, 77.36, 46.87, 28.02, 26.94, 25.01.

HRMS (MALDI-TOF): m/z calculated for $C_{48}H_{42}BN_4O_2$ $[M+H]^+$: 717.3395; Found: 717.3399.

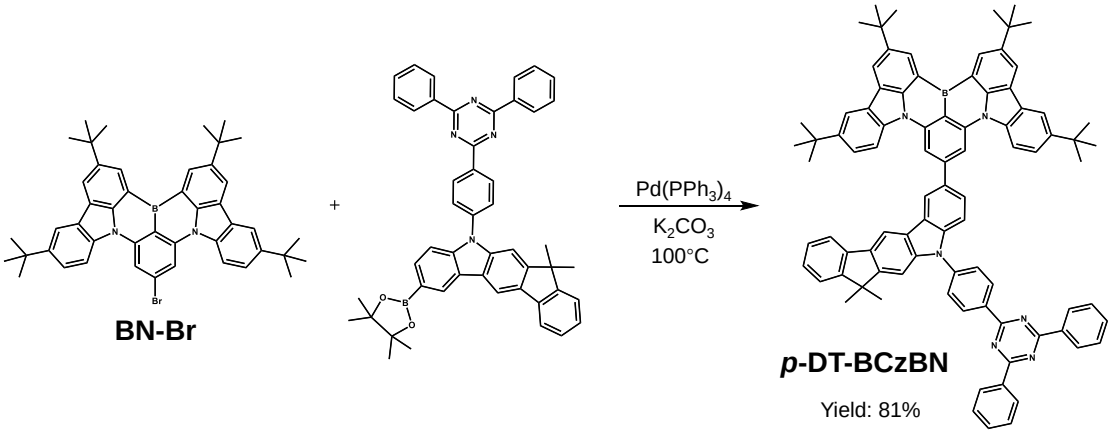

Scheme S8. Synthesis route of *p*-DT-BCzBN.

BN-Br (0.63 g, 0.88 mmol), **DMIC-*p*-TRZ-Bpin** (0.57 g, 0.80 mmol), $Pd(PPh_3)_4$ (0.046 g, 0.04 mmol), K_2CO_3 (0.17 g, 1.2 mmol) were dissolved in anhydrous toluene (30 mL) / deionized water (10 mL) under a nitrogen atmosphere. After stirring at 100 °C for 24 h, the reaction was cooled down to room temperature. Then the mixture was extracted with dichloromethane/water for three times, and then organic layer was dehydrated with anhydrous magnesium sulfate. After filtering and drying, crude product could be obtained. The crude product was purified by column chromatography (the eluent was dichloromethane: petroleum ether = 1:5), and the bright yellow powder (0.80 g) was obtained with a yield of 81%.

^{1}H NMR (400 MHz, Chloroform-*d*) δ 9.13 (d, *J* = 1.9 Hz, 2H), 9.06 (d, *J* = 8.2 Hz, 2H), 8.82 – 8.76 (m, 4H), 8.70 (d, *J* = 1.5 Hz, 1H), 8.63 (s, 3H), 8.53 – 8.45 (m, 4H), 8.28 (d, *J* = 2.0 Hz, 2H), 8.05 – 7.98 (m, 1H), 7.92 (t, *J* = 7.1 Hz, 3H), 7.76 (d, *J* = 8.4 Hz, 1H), 7.70 – 7.54 (m, 9H), 7.46 (d, *J* = 7.3 Hz, 1H), 7.39 (td, *J* = 7.4, 1.1 Hz, 1H), 7.31 (td, *J* = 7.3, 1.0 Hz, 1H), 1.69 (s, 18H), 1.57 (s, 6H), 1.53 (s, 18H).

^{13}C NMR (101 MHz, Chloroform-*d*) δ 171.78, 170.83, 153.82, 153.40, 147.20, 145.29, 144.74, 144.60, 141.82, 141.54, 141.39, 140.91, 139.45, 138.40, 136.07, 135.22, 134.82, 133.20, 132.68, 130.83, 129.84, 129.01, 128.69, 127.19, 126.86, 126.58, 126.09, 124.83, 124.44, 123.60, 123.43, 122.61, 121.80, 121.79, 121.75, 120.56, 119.62, 119.58, 117.32, 114.25, 111.78, 110.61, 107.66, 104.40, 46.93, 35.21, 34.83, 32.25, 31.86, 27.99.

MS (MALDI-TOF): m/z calculated for $C_{88}H_{77}BN_6$ $[M]^+$: 1228.6303; Found: 1228.3008.

S6. Thermal analysis

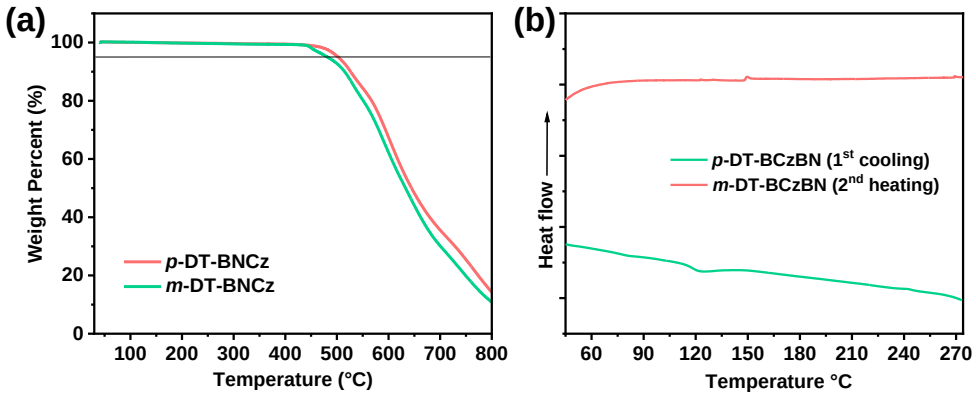

Figure S1. (a) The thermogravimetric analysis curves of both emitters and (b) the differential scanning calorimetry curves (endotherm up).

S7. Quantum chemical calculation

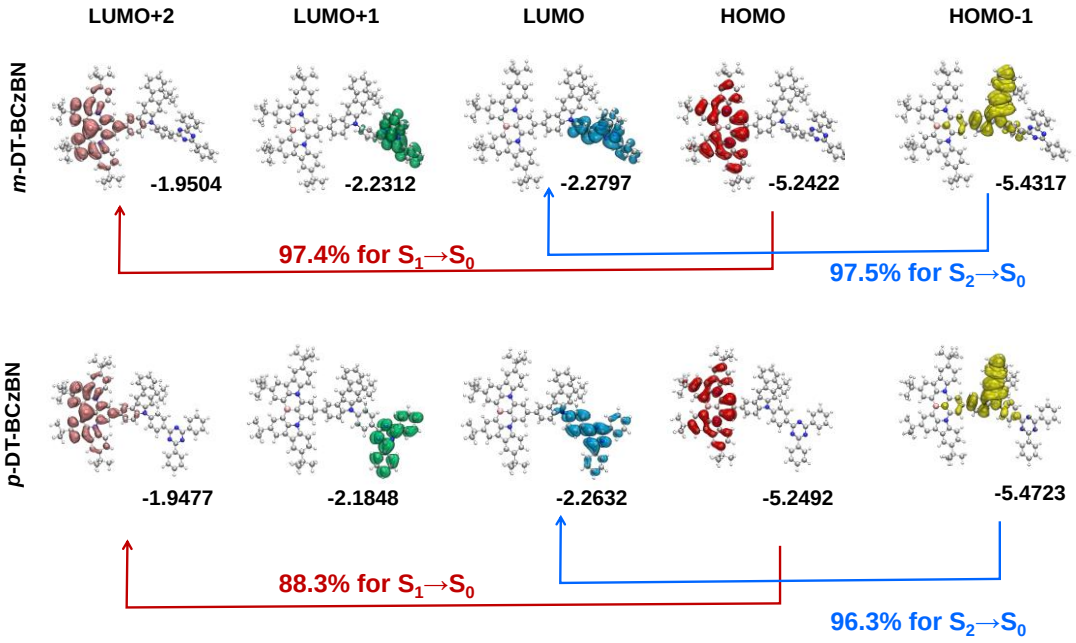

Figure S2. The molecualr orbital distributions of ground states for *m*-DT-BCzBN and *p*-DT-BCzBN.

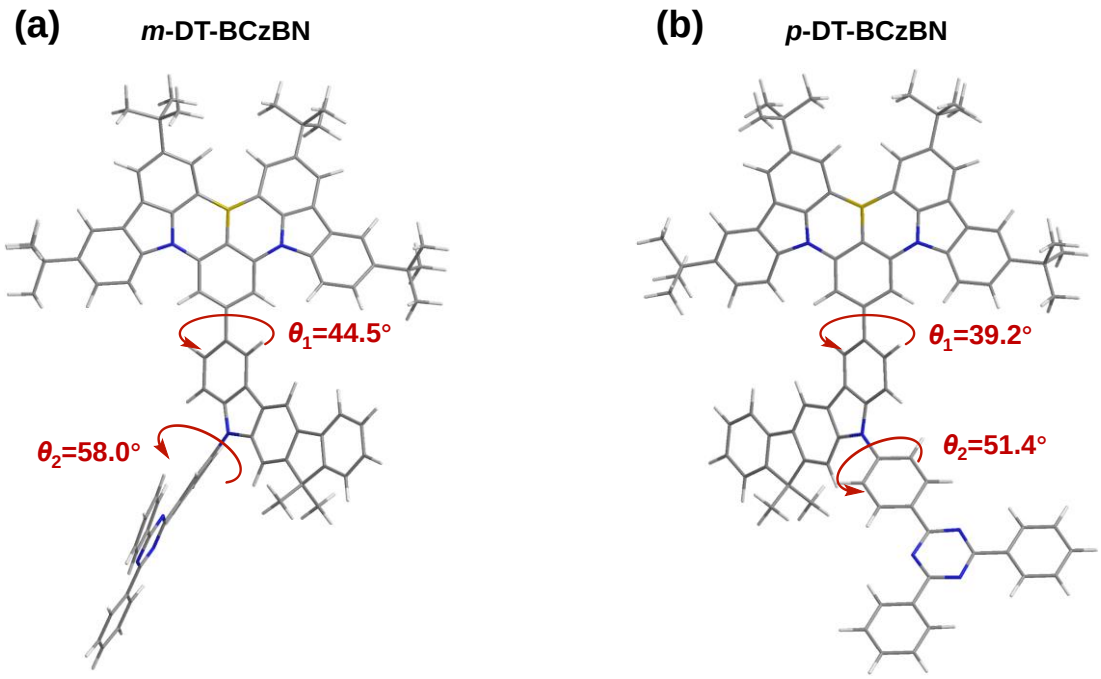

Figure S3. The optimized molecular structures and twisted angles of m-DT-BCzBN and p-DT-BCzBN.

S8. Photophysical analysis

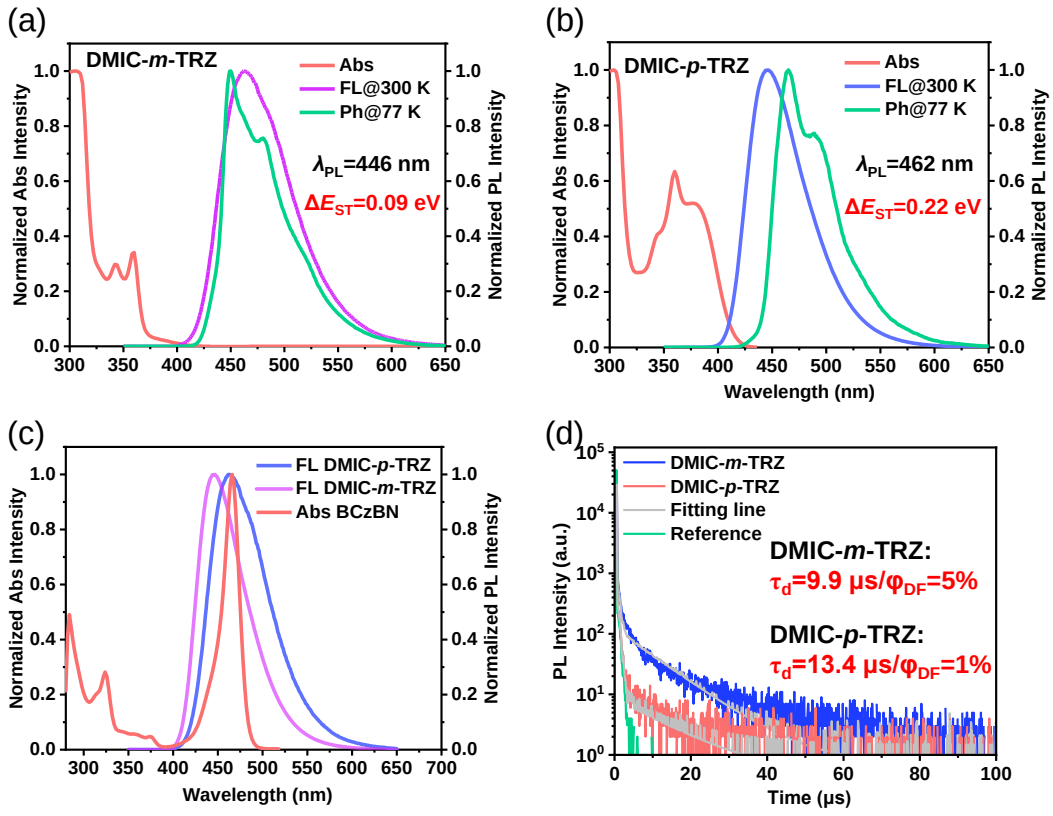

Figure S4. The absorption spectra, PL spectra at 300 K and phosphorescence spectra at of (a) DMIC-*m*-TRZ in toluene, and (b) DMIC-*p*-TRZ in toluene. (c) The overlap between the absorption spectrum and the PL spectra of DMIC-*m*/*p*-TRZ emitters. (d) The transient PL decay curves of 2 wt% DMIC-*m*/*p*-TRZ doped in PhCzBCz.

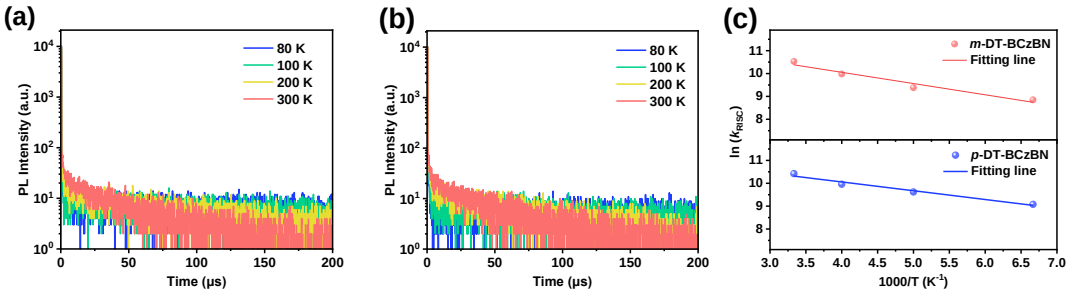

Figure S5. Temperature-dependent transient PL decay curves of (a) *m*-DT-BCzBN and (b) *p*-DT-BCzBN based the doped films in vacuum. (c) The Arrhenius plots of the temperature dependence of k_{RISC} for the doped films.

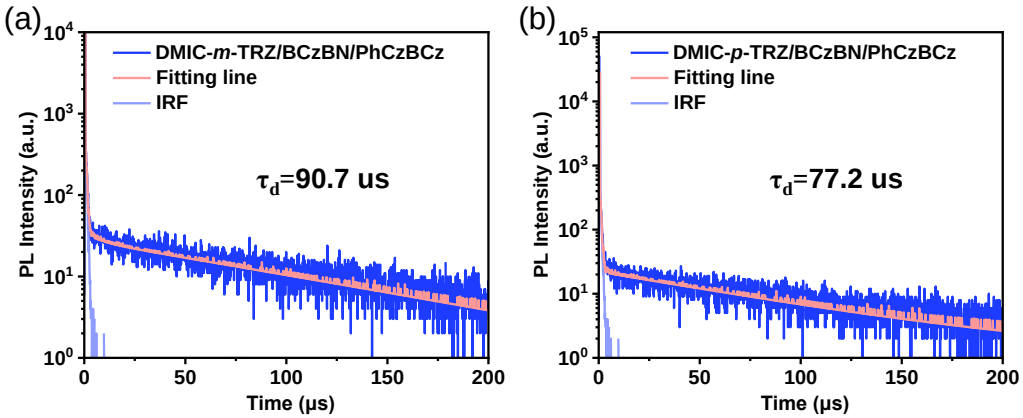

Figure S6. The transient PL spectra using DMIC-m/p-TRZ, BCzBN, and PhCzBCz based ternary blended films under vacuum.

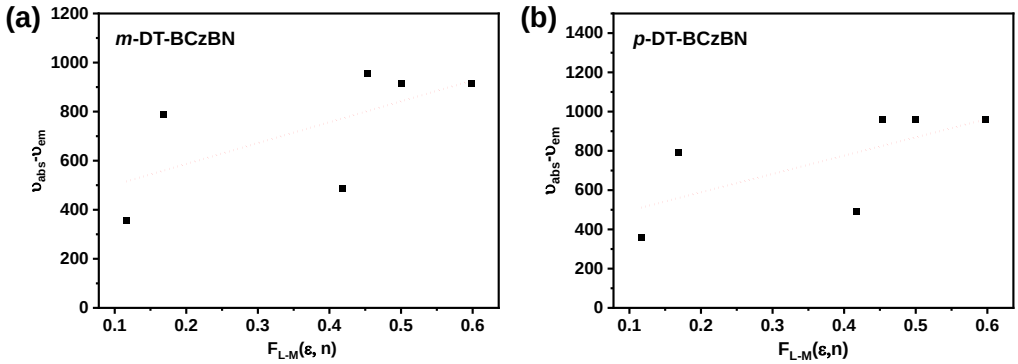

Figure S7. Lippert-Mataga plot (ν_{abs}-ν_{em} against orientation polarizability of solvent) of (a) *m*-DT-BCzBN, and (b) *p*-DT-BCzBN.

S9. Electrochemical analysis

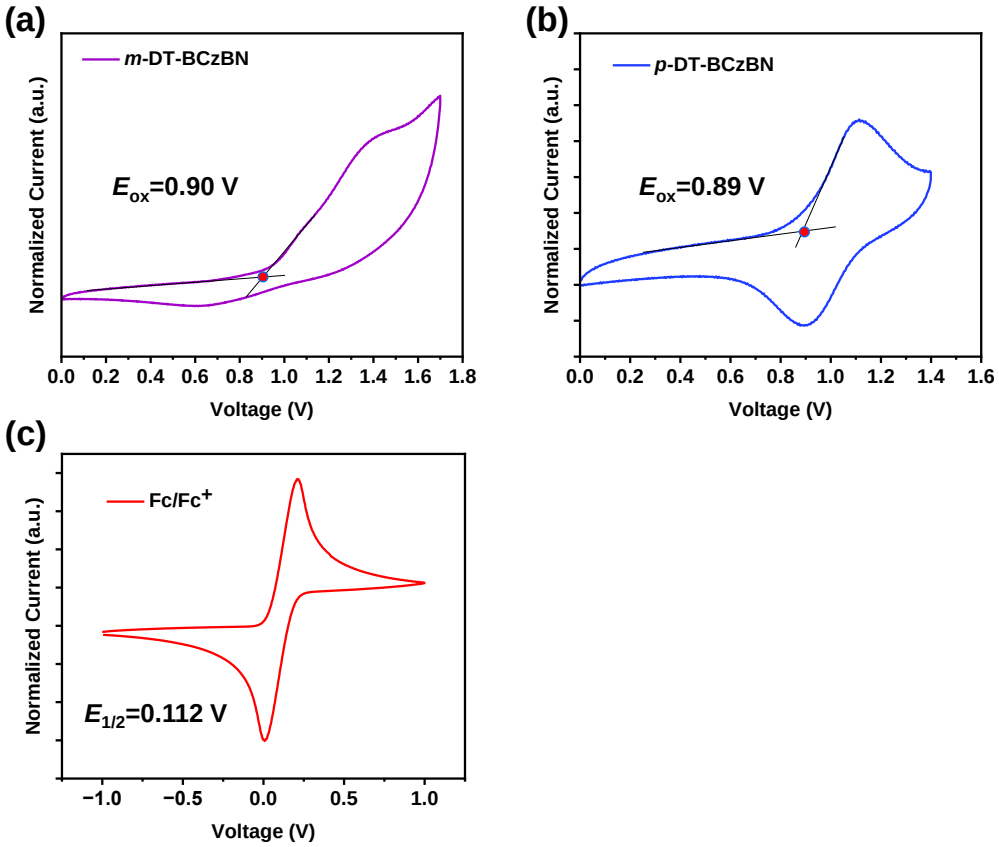

Figure S8. The cyclic voltammetry curves of the emitters and ferrocene as the external reference.

S10. OLED performance

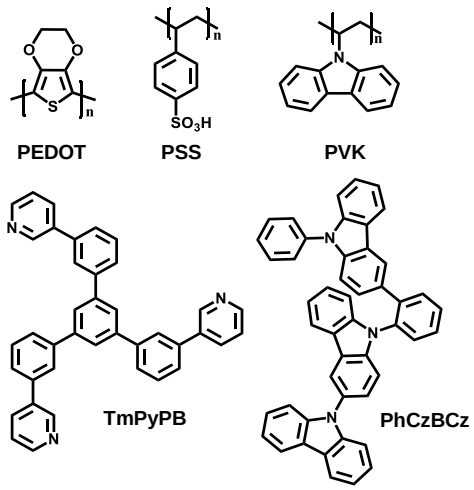

Scheme S9. The molecular structures of the functional materials.

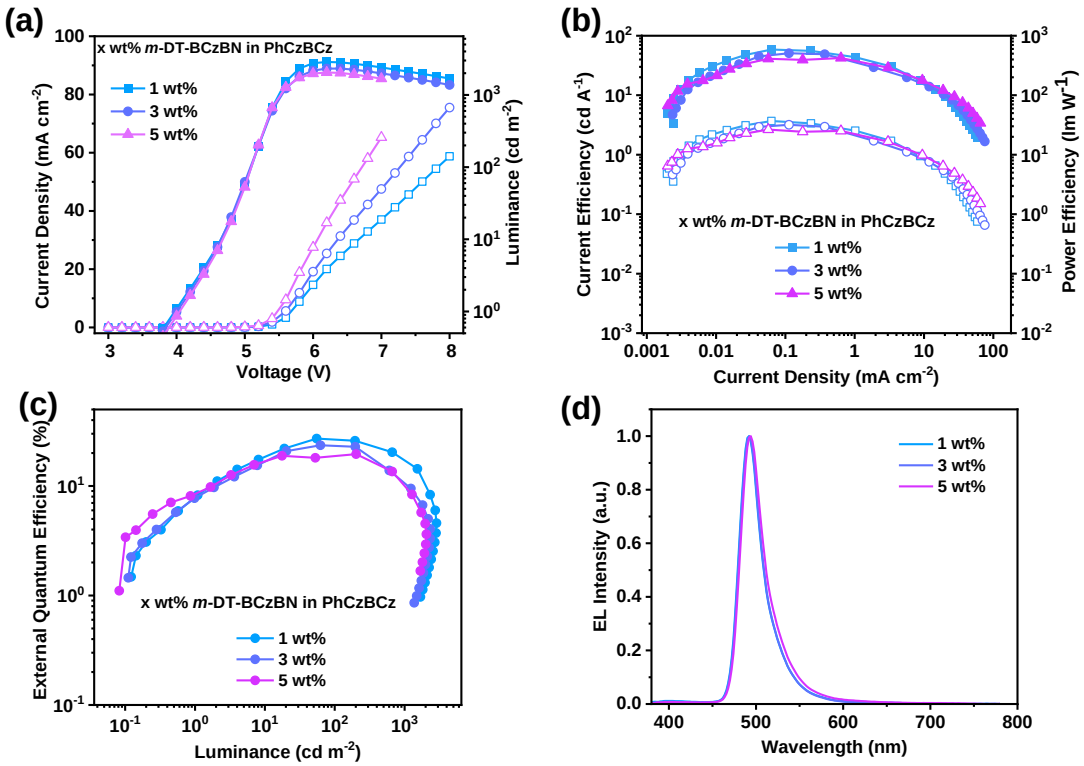

Figure S9. Device performance of *m*-DT-BCzBN based solution-processed OLEDs at different doping concentrations. (a) Luminance−voltage−current density curves; (b) Current efficiency− current density−power efficiency curves; (c) External quantum efficiency versus luminance curves; (d) The EL spectra.

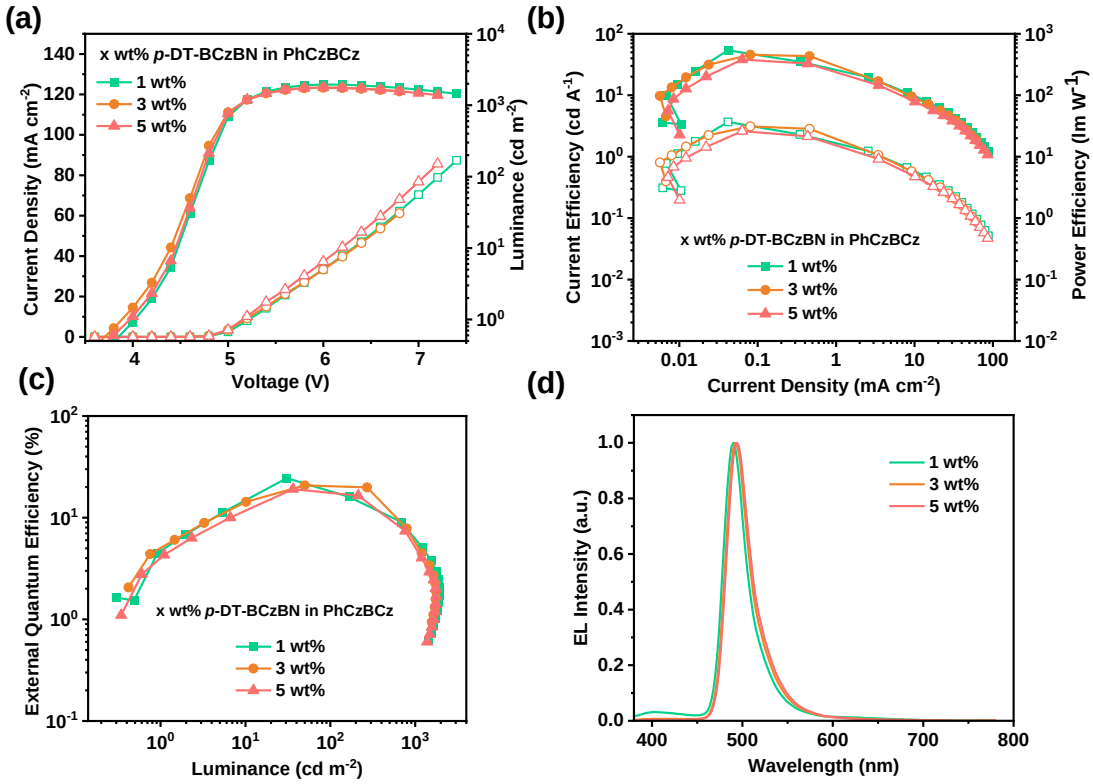

Figure S10. Device performance of *p*-DT-BCzBN based solution-processed OLEDs at different doping concentrations. (a) Luminance−voltage−current density curves; (b) Current efficiency− current density−power efficiency curves; (c) External quantum efficiency versus luminance curves; (d) The EL spectra.

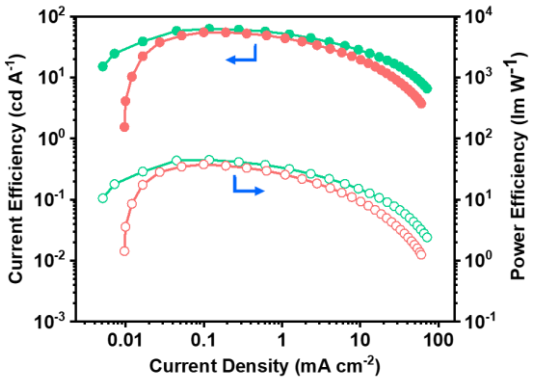

Figure S11. The maximum current efficiency (CE_{max}) and power efficiency (PE_{max}) for *m*-DT-BCzBN (green line) and *p*-DT-BCzBN (red line) based devices.

S11. NMR and MS results

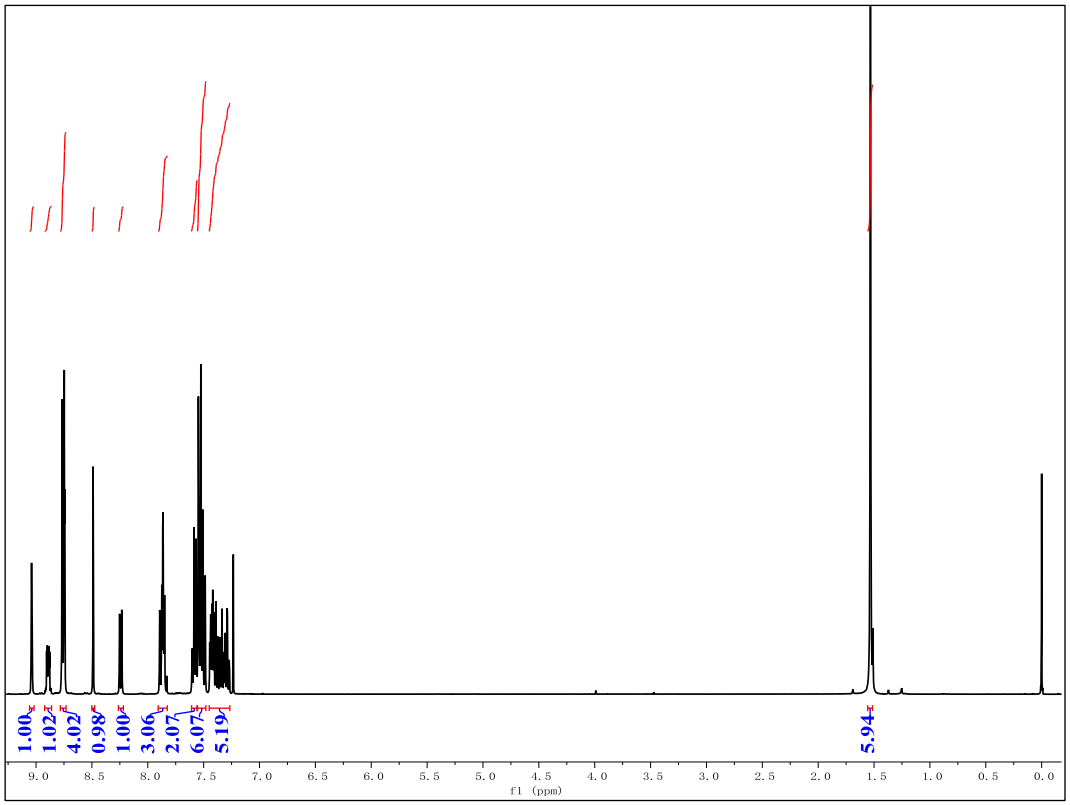

Figure S12. The ^{1}H NMR spectrum of DMIC-*m*-TRZ.

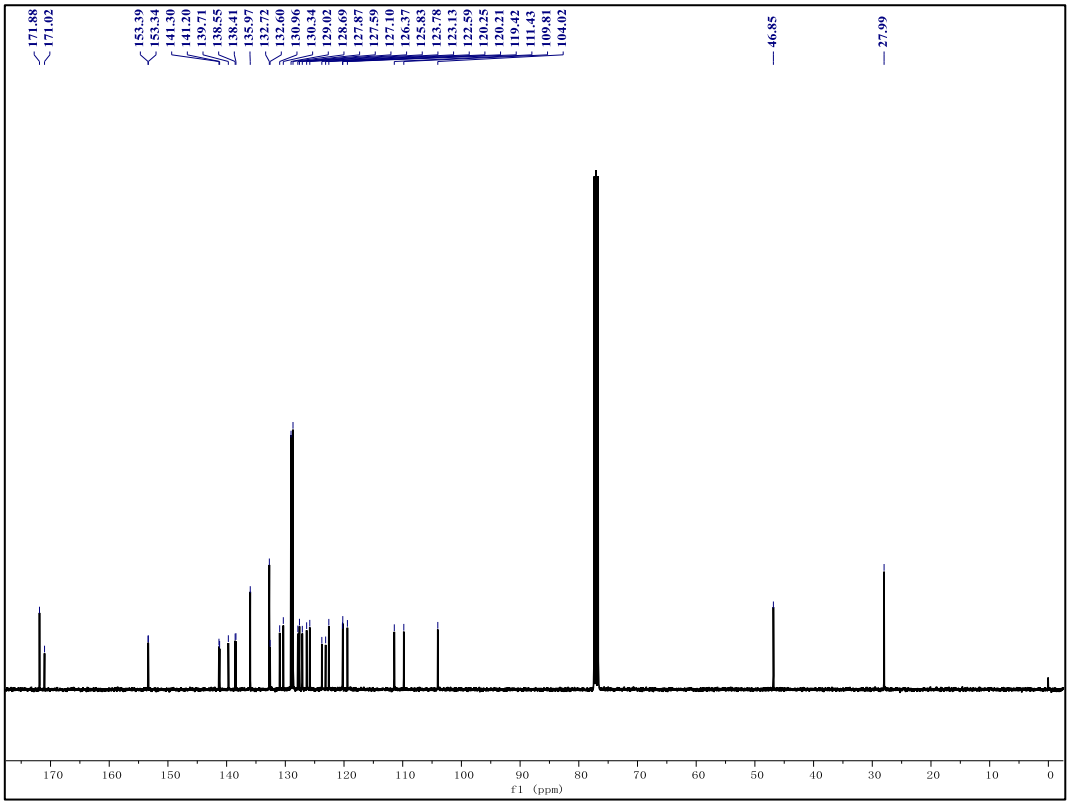

Figure S13. The ^{13}C NMR spectrum of DMIC-*m*-TRZ.

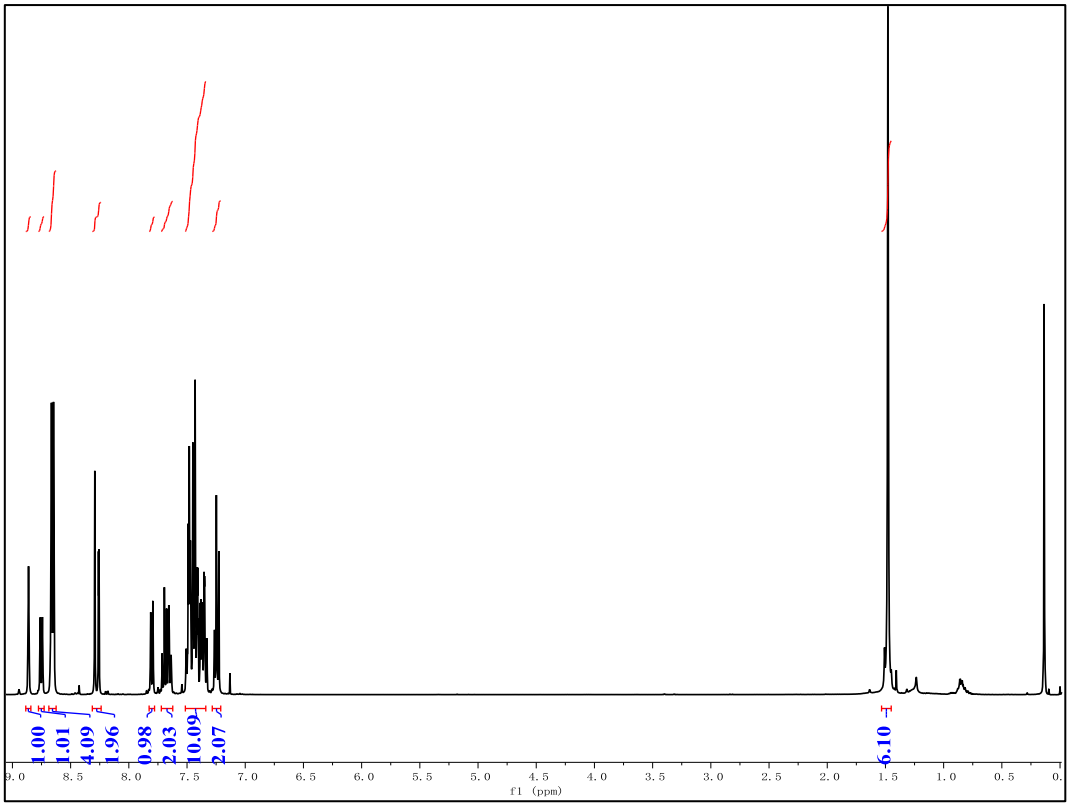

Figure S14. The ^{1}H NMR spectrum of DMIC-*m*-TRZ-Br.

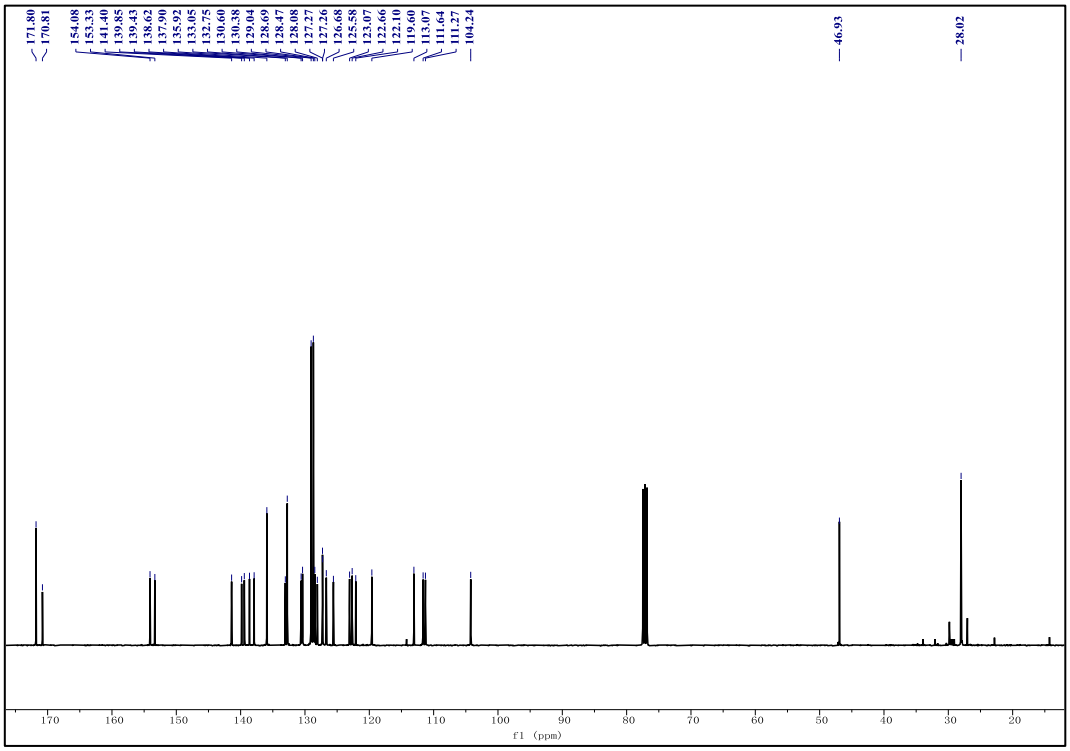

Figure S15. The ^{13}C NMR spectrum of DMIC-*m*-TRZ-Br.

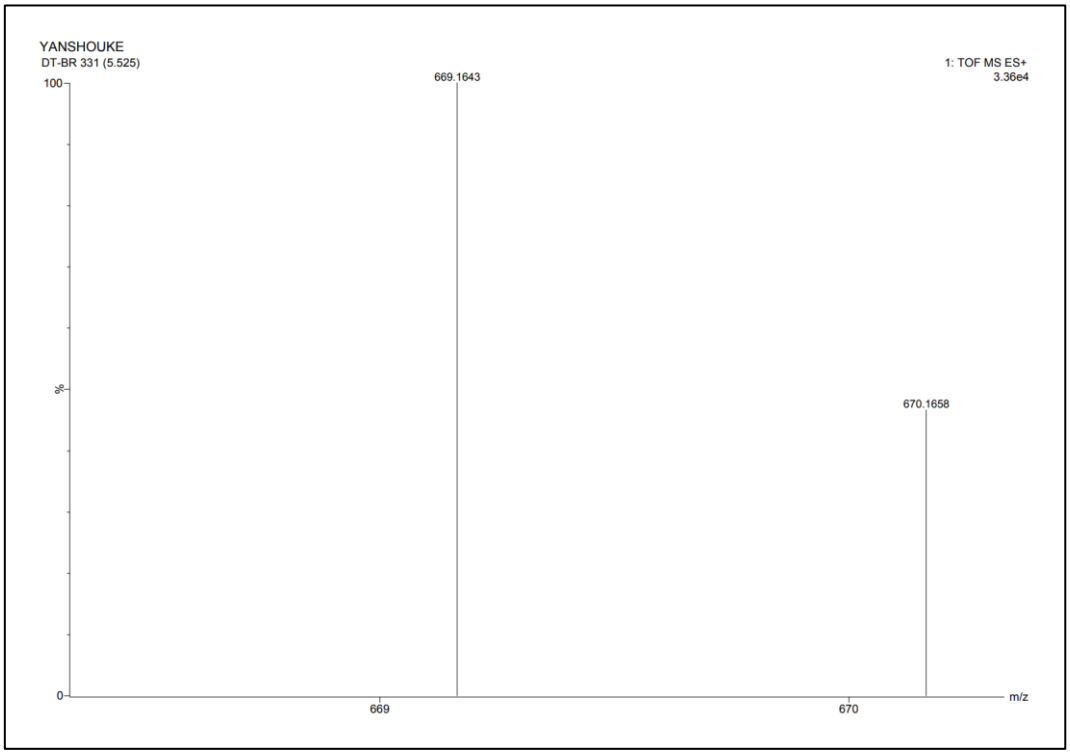

Figure S16. The MALDI-TOF-MS spectrum of DMIC-*m*-TRZ-Br.

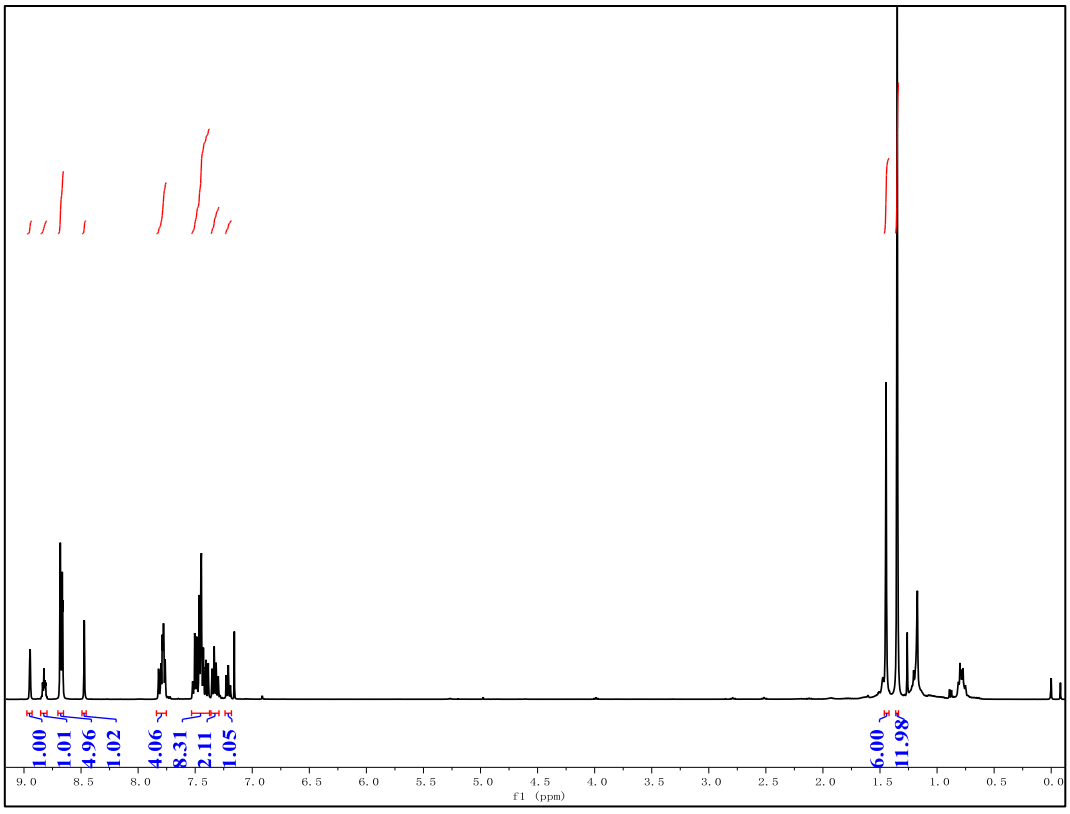

Figure S17. The ^{1}H NMR spectrum of DMIC-*m*-TRZ-Bpin.

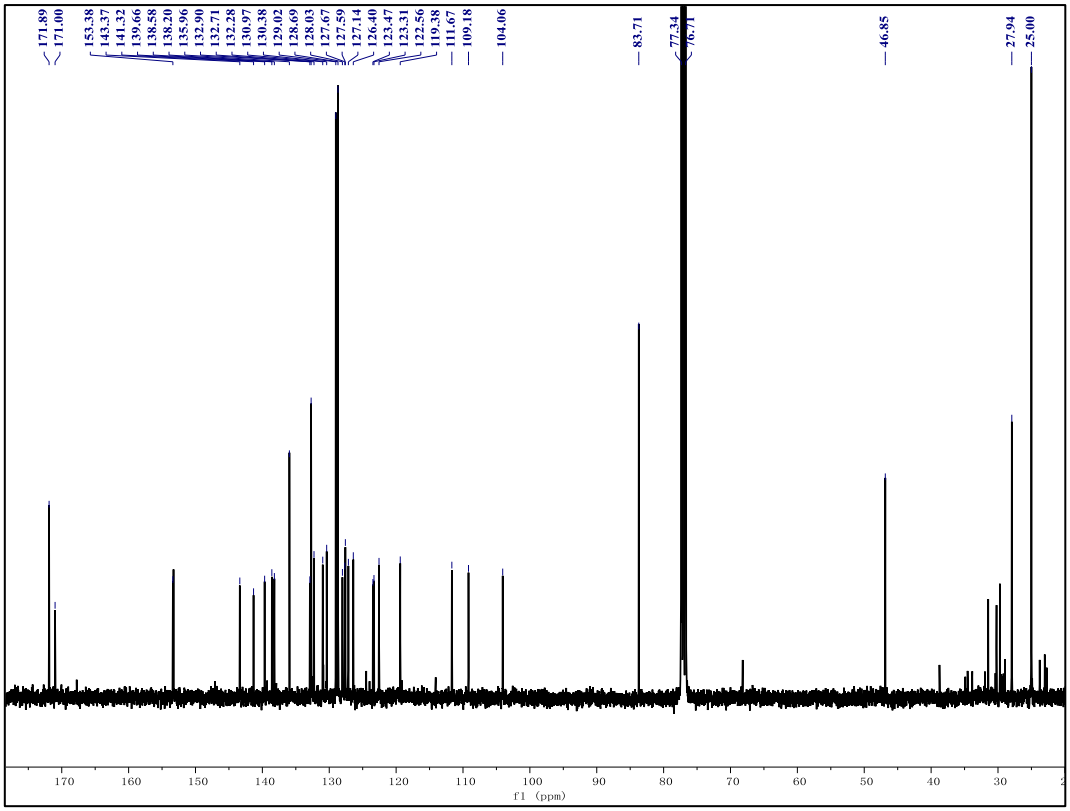

Figure S18. The ^{13}C NMR spectrum of DMIC-*m*-TRZ-Bpin.

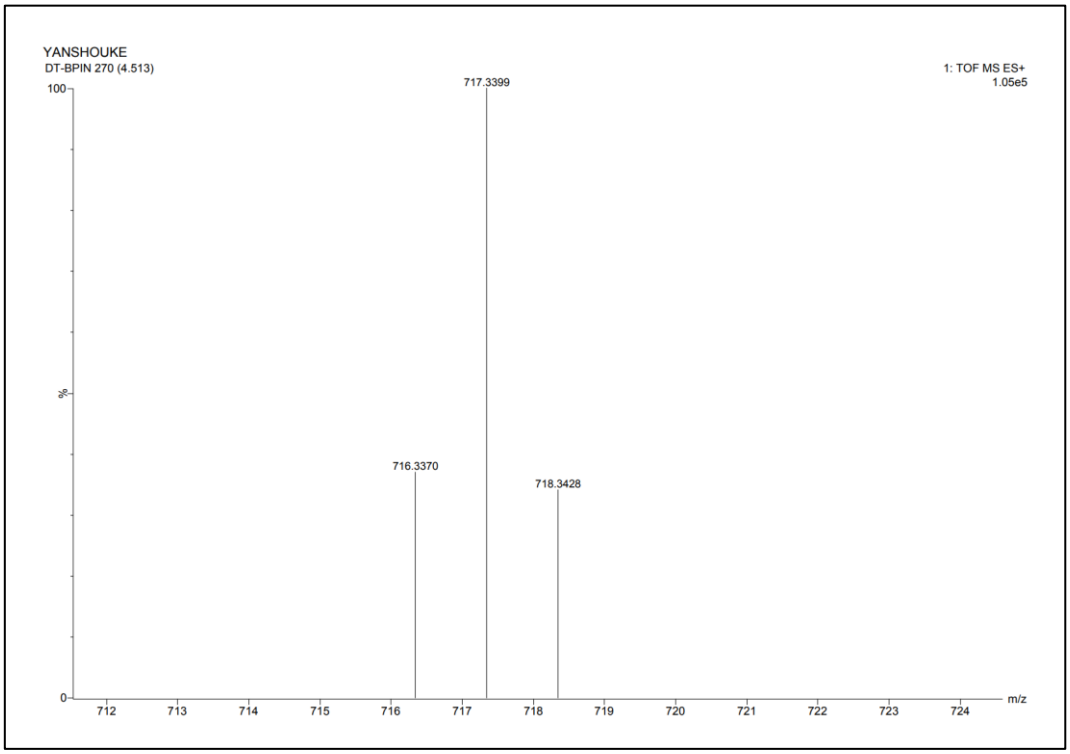

Figure S19. The MALDI-TOF-MS spectrum of DMIC-*m*-TRZ-Bpin.

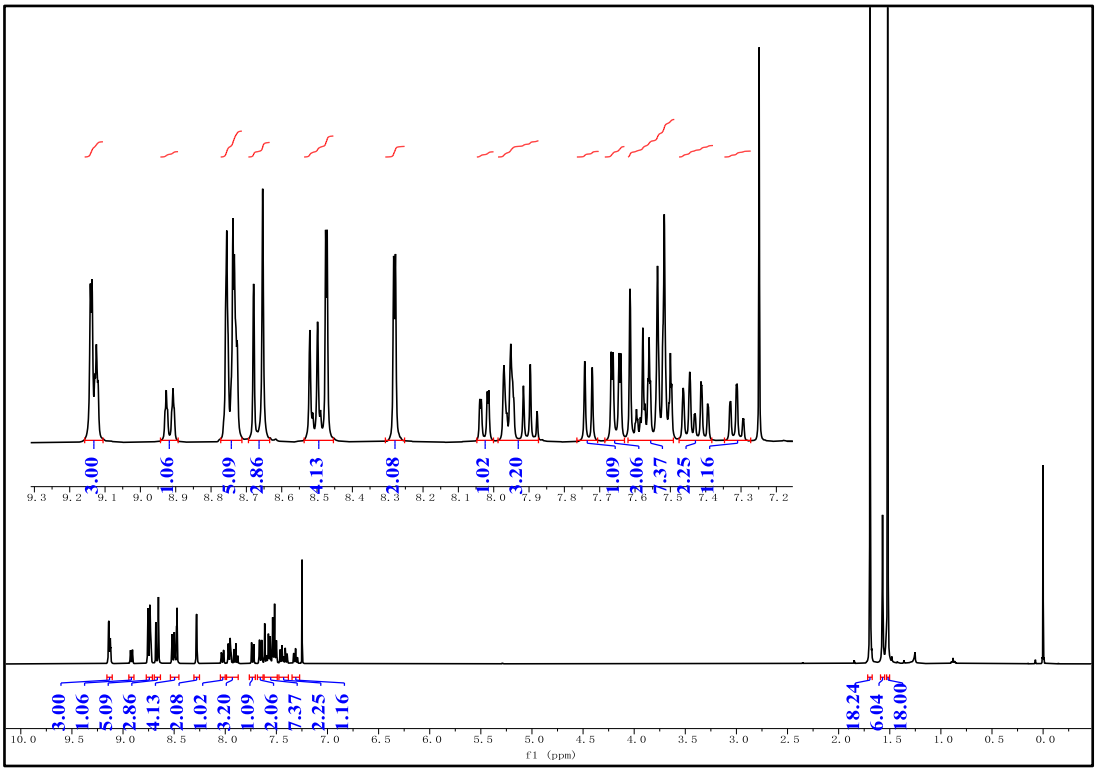

Figure S20. The ^{1}H NMR spectrum of *m*-DT-BCzBN.

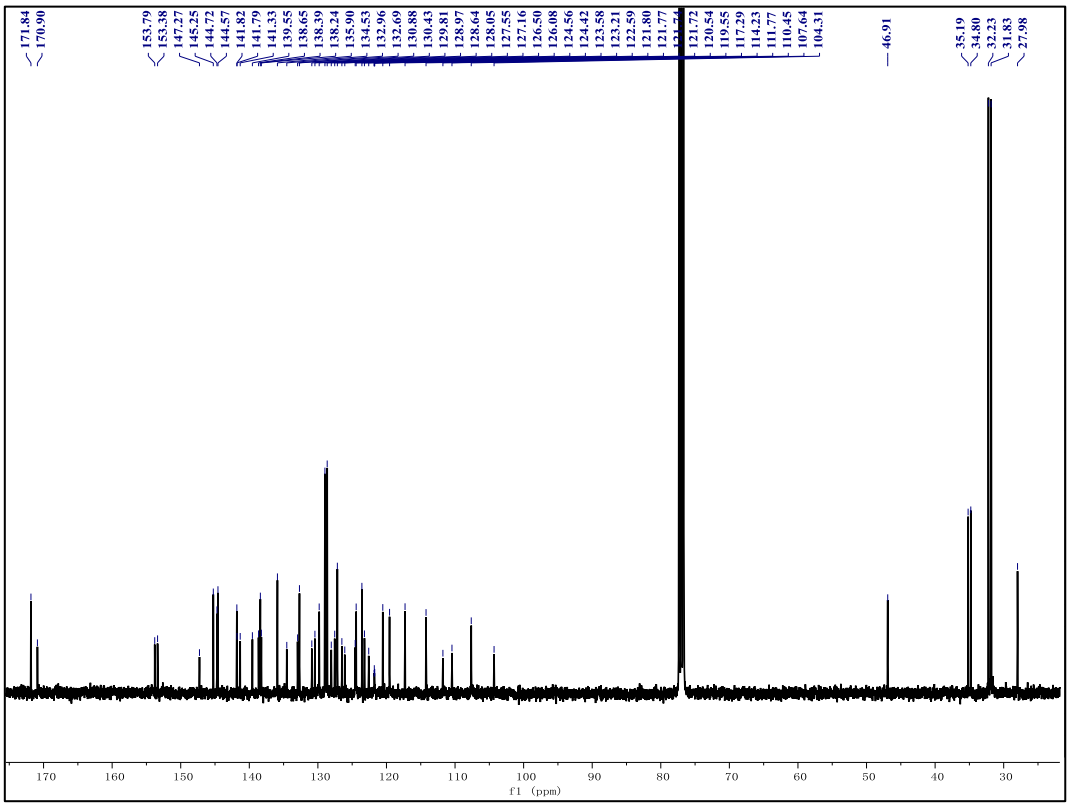

Figure S21. The ^{13}C NMR spectrum of *m*-DT-BCzBN.

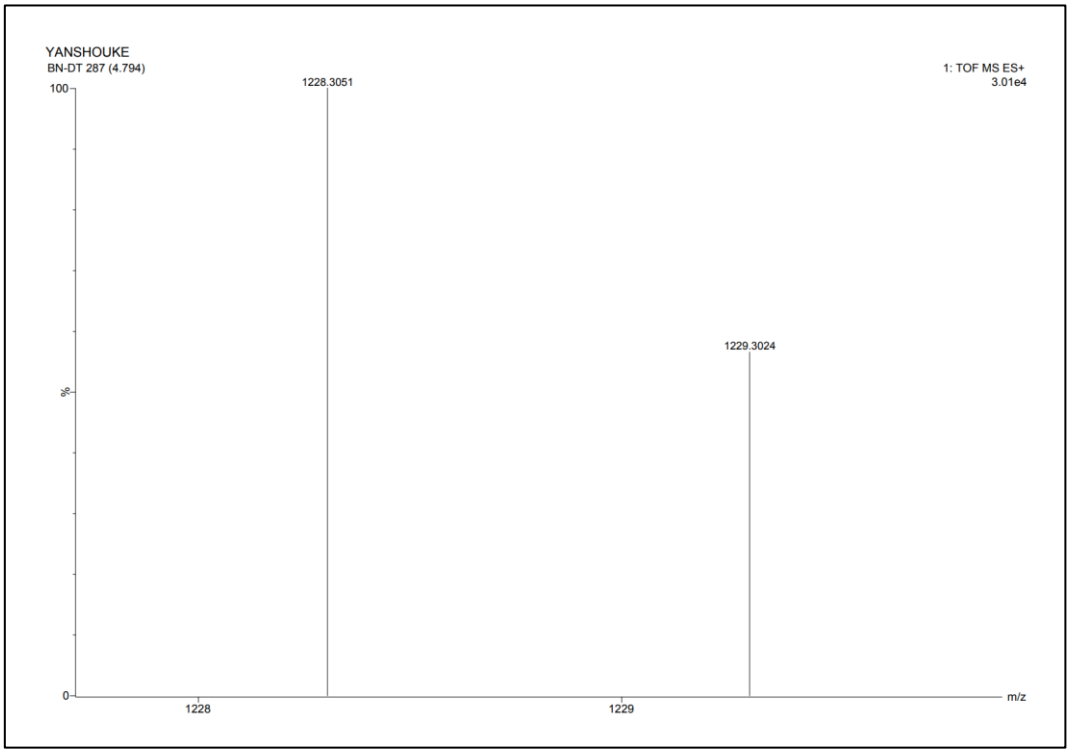

Figure S22. The MALDI-TOF-MS spectrum of *m*-DT-BCzBN.

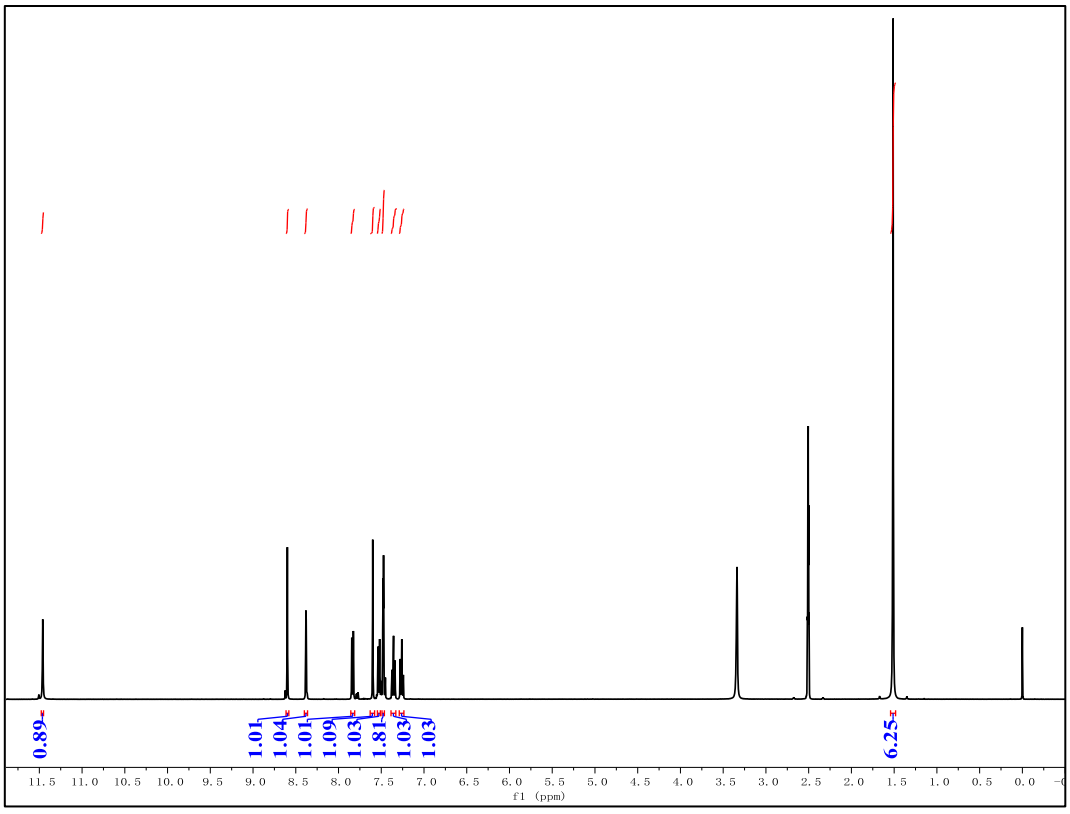

Figure S23. The ^{1}H NMR spectrum of 2-bromo-5,7-dihydro-7,7-dimethylindeno[2,1-b]carbazole.

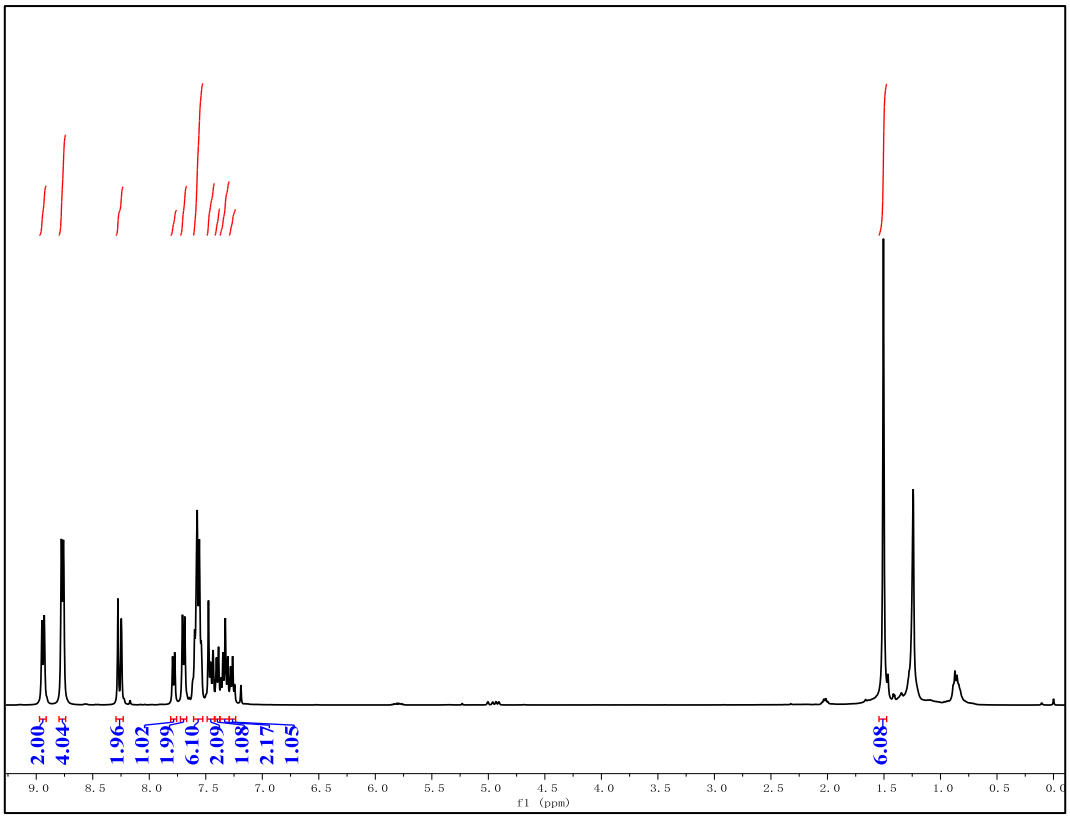

Figure S24. The ^{1}H NMR spectrum of DMIC-*p*-TRZ-Br.

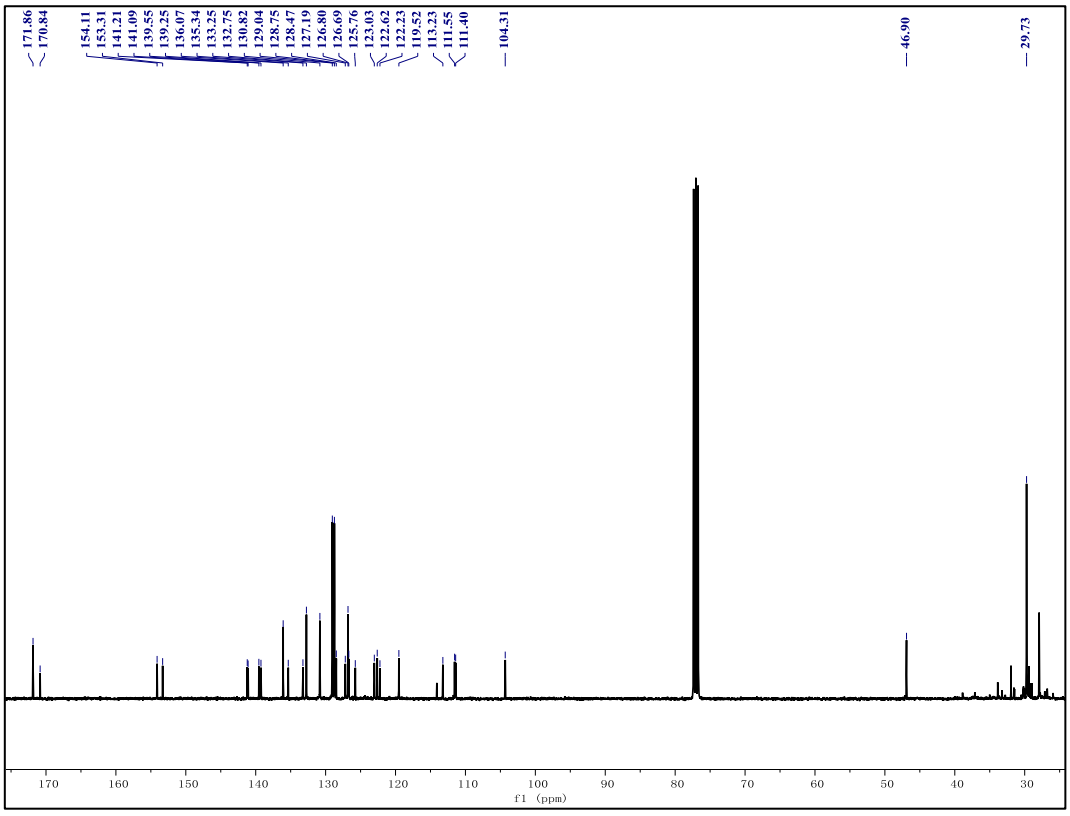

Figure S25. The ^{13}C NMR spectrum of DMIC-*p*-TRZ-Br.

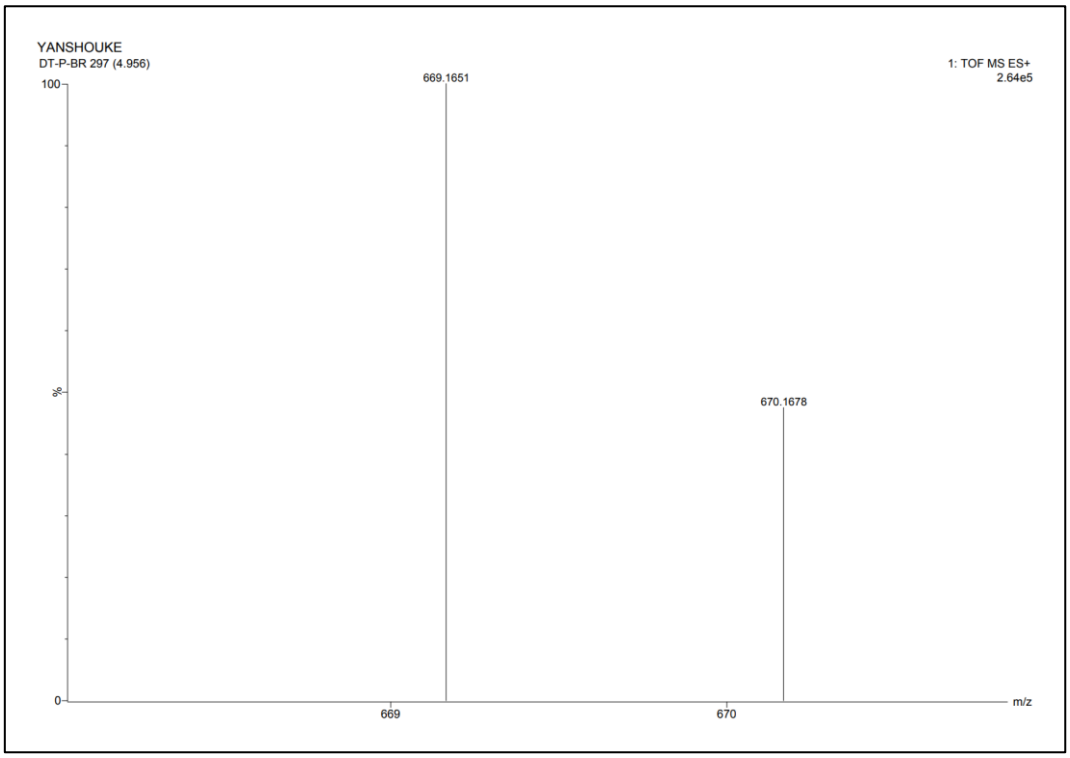

Figure S26. The MALDI-TOF-MS spectrum of DMIC-*p*-TRZ-Br.

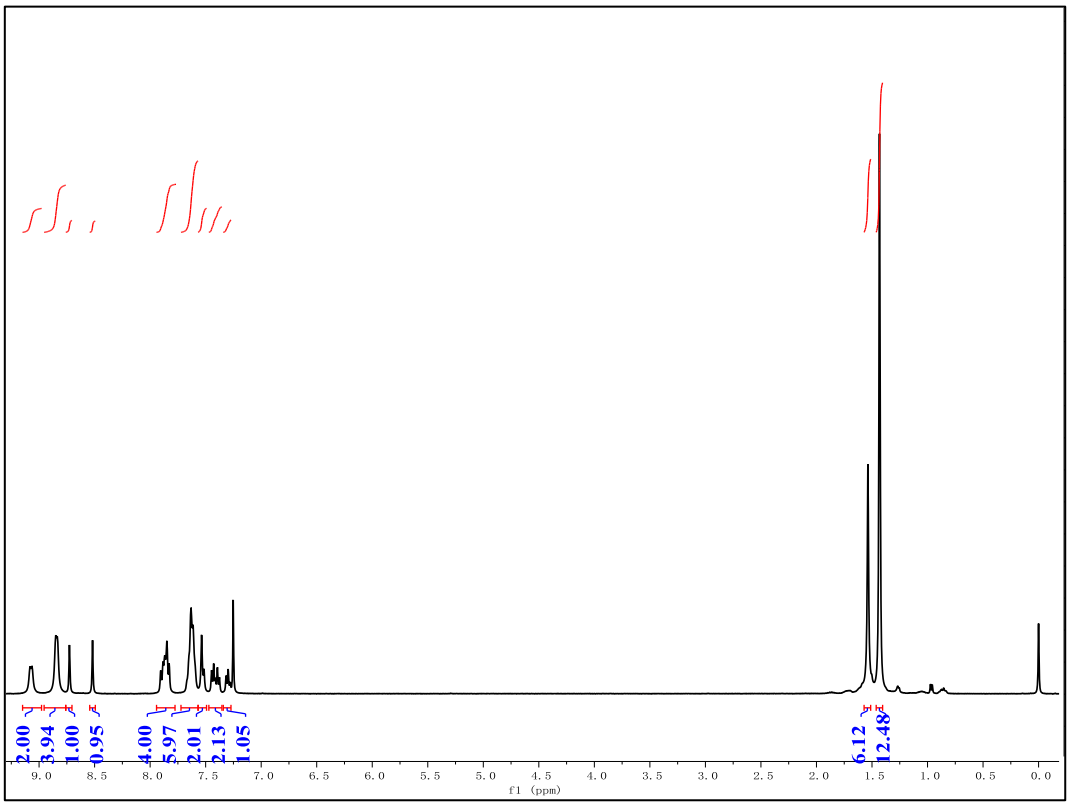

Figure S27. The ^{1}H NMR spectrum of DMIC-*p*-TRZ-Bpin.

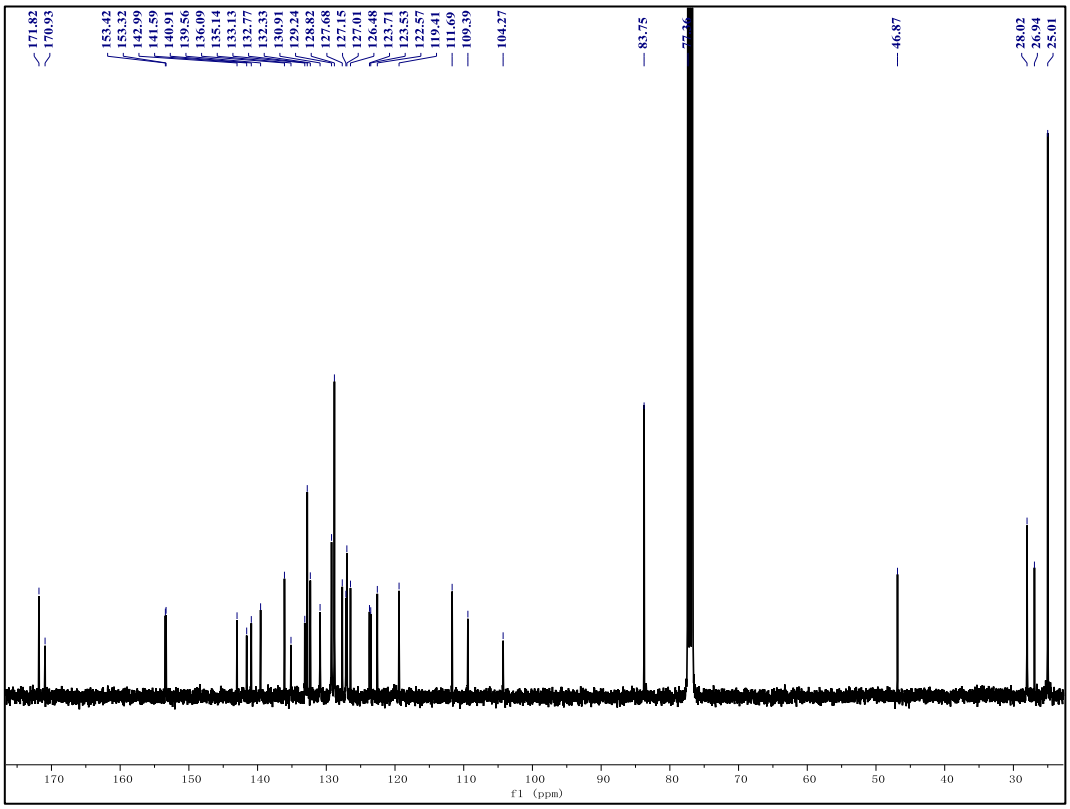

Figure S28. The ^{13}C NMR spectrum of DMIC-*p*-TRZ-Bpin.

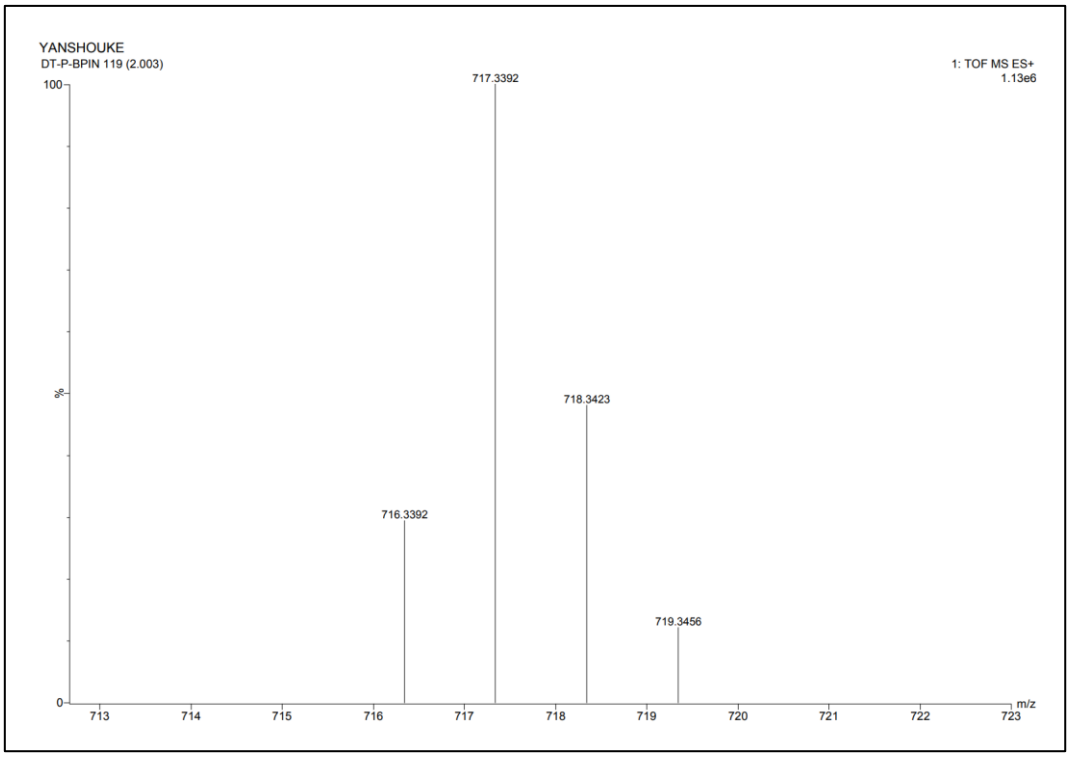

Figure S29. The MALDI-TOF-MS spectrum of DMIC-*p*-TRZ-Bpin.

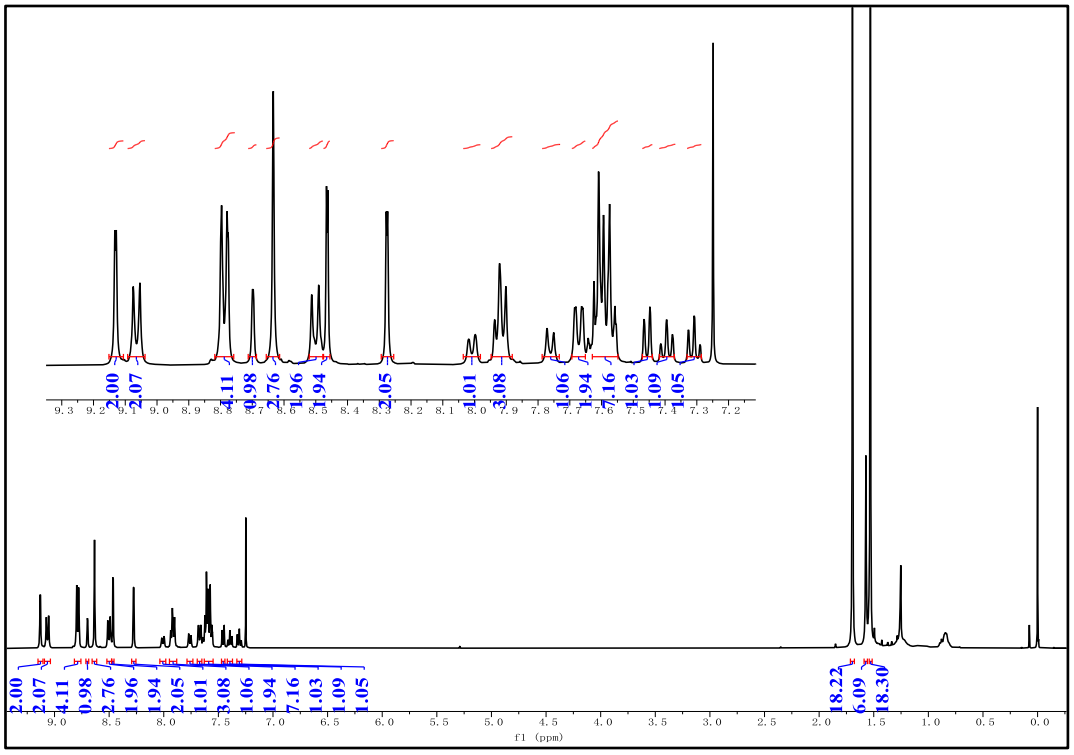

Figure S30. The ^{1}H NMR spectrum of *p*-DT-BCzBN.

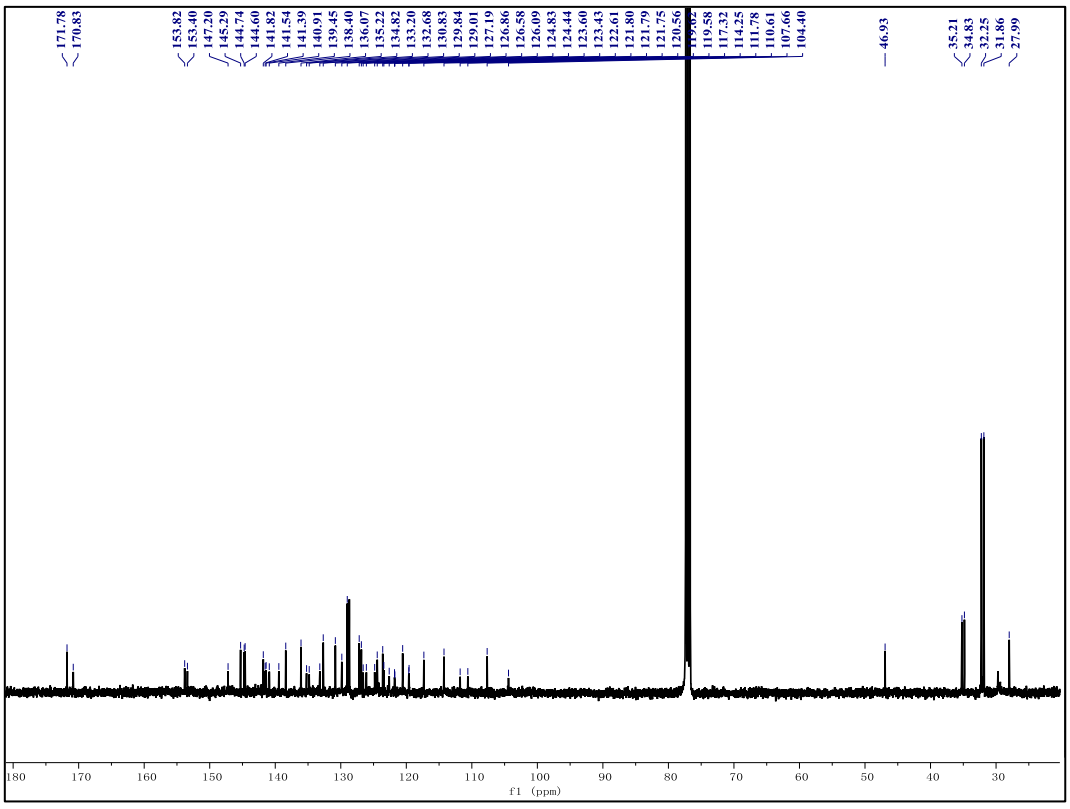

Figure S31. The ^{13}C NMR spectrum of *p*-DT-BCzBN.

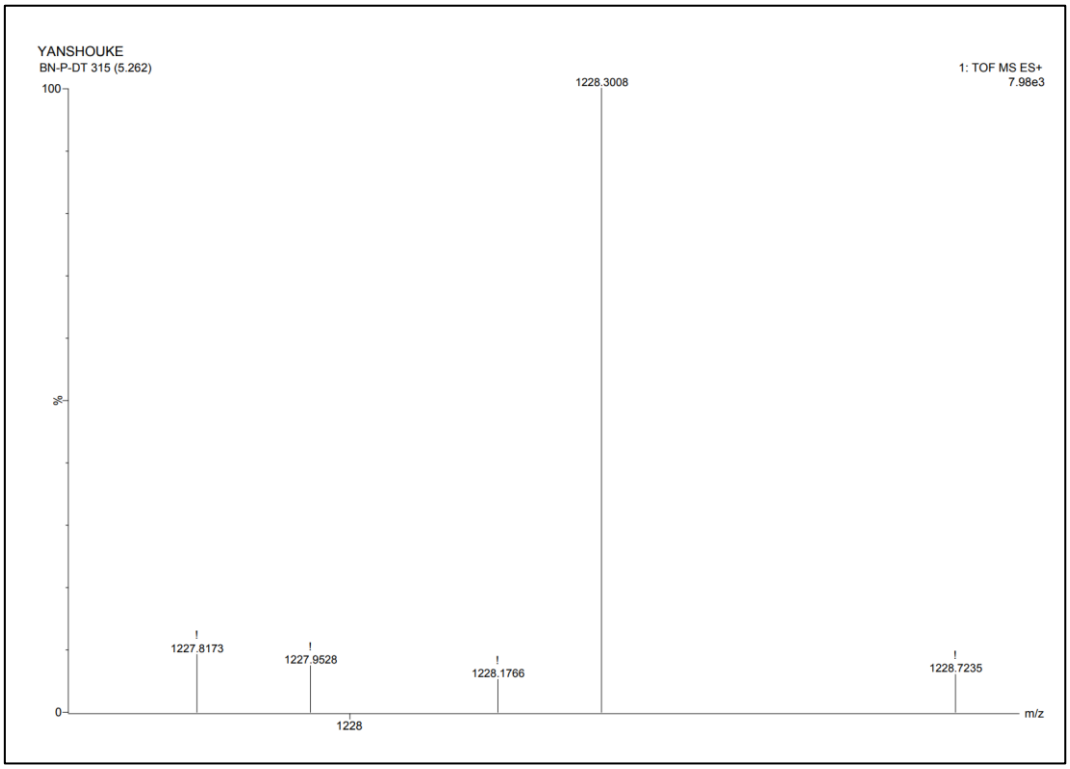

Figure S32. The MALDI-TOF-MS spectrum of *p*-DT-BCzBN.

S12. Reference

[1] Y. Liu, Y. Wang, C. Li, Z. Ren, D. Ma, S. Yan, *Macromolecules* 2018, **51**, 4615.

[2] W. L. Tsai, M. H. Huang, W. K. Lee, Y. J. Hsu, K. C. Pan, Y. H. Huang, H. C. Ting, M. Sarm, Y. Y. Ho, H. C. Hu, C. C. Chen, M. T. Lee, K. T. Wong, C. C. Wu, *Chem. Commun.* 2015, **51**, 13662.

[3] Y. Liu, G. Xie, Z. Ren, S. Yan, *ACS Appl. Polym. Mater*. 2019, **8**, 2204.

[4] T. Lu, F. Chen, *Acta Chim. Sinica* 2011, **69**, 2393–2406.

[5] T. Lu, F. Chen, *J. Comput. Chem.* 2012, **33**, 580–592.

[6] Z. Pei, Q. Ou, Y. Mao, J. Yang, A. Lande, F. Plasser, W. Liang, Z. Shuai, Y. Shao, *J. Phys. Chem. Lett.* 2021, **12**, 2712−2720.

[7] X. Chen, S. Zhang, J. Fan, A. Ren, *J. Phys. Chem. C* 2015, **119**, 9728–9733.